Atmospheric
Chemistry
and Physics

Supplement of

Measurement report: Elevated atmospheric ammonia may promote particle pH and HONO formation – insights from the COVID-19 pandemic

Xinyuan Zhang et al.

Correspondence to: Shenbo Wang (shbwang@zzu.edu.cn) and Ruiqin Zhang (rqzhang@zzu.edu.cn)

S1. Detailed description of the aerosol and gas monitor.

The aerosol and gas monitor (MARGA, Metrohm, Switzerland) was used to analyze the hourly water-soluble ions (Na^+, NH_4^+, K^+, Mg^{2+}, Ca^{2+}, Cl^-, NO_3^-, and SO_4^{2-}) in $PM_{2.5}$, as well as gaseous species (NH_3, HNO_3, HCl, and $HONO$) at ten sampling sites. The atmospheric sample passes through a $PM_{2.5}$ cut-off head, and both particles and gases enter a wet rotating dissolution device for diffusion. Subsequently, the particles in the sample undergo hygroscopic growth and condensation in an aerosol supersaturated vapor generator, followed by collection and ion chromatographic analysis. The gases in the sample are oxidized by H_2O_2 in the dissolution device, absorbed into a liquid solvent, and then entered the gas sample collection chamber for ion chromatographic quantification. During this process, the sample is extracted through a liquid diffusion filter, where interfering acidic and alkaline gases are removed. To achieve high collection efficiency, the airflow containing loaded ions then enters an aerosol supersaturated collector until the particles can be injected into the ion chromatograph. The ion chromatography system utilizes either suppressor or non-suppressor conductivity detection methods for ion analysis. Before running the samples, the ion chromatograph system needs to be calibrated using standard solutions. By comparing the data obtained from the sample with the data obtained from known standard solutions, the identification and quantification of sample ions can be performed. The data acquisition system generates chromatograms, and the

21   chromatography software further converts each peak in the chromatogram into sample

22   concentrations and outputs the results.

23   **QA/QC**

24   The instrument underwent daily checks and maintenance, which typically involved

25   ensuring the stability of the internal standard response and maintaining a relative error

26   within ±10% between the measured and theoretical concentrations of the internal

27   standard. The system's data acquisition and transmission were carefully examined,

28   along with monitoring the instrument's status information and collected data. This

29   included checking parameters such as sampling flow rate, chromatographic column

30   pressure, column temperature, conductivity, target compound peak retention time, and

31   peak width to ensure their normal functioning. Regular replacement of consumables

32   used by the instrument was carried out at predetermined intervals and frequencies.

33   Additionally, standard curve measurements and calibration were performed in each

34   season to guarantee the accuracy of the instrument's data. Calibration curve verification

35   was performed at least once per quarter. A standard series containing at least 6

36   calibration points, including zero concentration, was prepared using standard solutions.

37   The concentration range of the calibration curve was set according to the actual

38   environmental concentration levels and determined by manual injection. The obtained

39   calibration curve had a linear correlation coefficient (r) of ≥0.995. If this requirement

40   was not met, the rationality of the internal standard solution concentration settings

41   would be checked. When key components such as the quantitative loop,

42 chromatographic column, or suppressor are replaced, a new calibration curve will be

43 promptly established. After establishing the new calibration curve, the sample sequence

44 in the analysis software would be updated. The minimum detection limit was

45 determined as follows: 0.002 μg/m^3 (Cl$^-$), 0.081 μg/m^3 (NH$_4^+$), 0.02 μg/m^3 (NO$_3^-$), 0.06

46 μg/m^3 (SO$_4^{2-}$), 0.002 μg/m^3 (Na$^+$), 0.08 μg/m^3 (K$^+$), 0.06 μg/m^3 (Ca^{2+}) and 0.007 μg/m^3

47 (Mg^{2+}). According to the research about the uncertainties in MARGA measurements,

48 such as a 20% uncertainty for MARGA measurements (Song et al., 2018), an error of

49 10% for detecting SO$_4^{2-}$, NO$_3^-$, and HNO$_3$, and 15% for NH$_3$ and NH$_4^+$ (Rumsey et al.,

50 2014), we set the uncertainties of 20% for NH$_3$ and NH$_4^+$ 10% for other components.

51 Due to the complex conditions encountered during the actual sampling process,

52 including variations in calibration slopes, sampling volumes, solvent concentrations,

53 temperature, atmospheric pressure, and sampling flow rates at different sampling points,

54 the assumed values mentioned above may not accurately reflect the actual situation.

S2. HONO measurement

The HONO monitoring method adopted in MARGA is the wet-flow diffusion tube method (WEDD) in the diffusion tube method (C.Zellweger, 1999;Takeuchi M, 2013), which is a common method for measuring HONO in wet chemistry and has high absorption efficiency. The device adopts a vertical setting, through the diffusion tube, the air in the atmosphere is pulled upward from the bottom, and the absorbent liquid is transported to the top of the diffusion tube through the air pump. When flowing under the action of gravity, a thin absorbent liquid film will be generated on the inner surface of the tube by the tension. The absorbent liquid film will absorb HONO, and the solution at the bottom of the diffusion tube will be sucked out through the air pump. Then it is sent to the ion chromatography for analysis. The integration time of the sample mainly depends on the running time of the ion chromatography, which is about 5-30 min (C.Zellweger, 1999;Takeuchi M, 2013). Based on the original, some scholars developed the flow injection-chemiluminescence method and used it together with WEDD for the measurement of HONO. The detection limit is about 0.03 $\mu g/m^3$ (Mikuska et al., 2008;Zhao et al., 2010). In addition, HONO observations measured with this AIM-IC system agree well with HONO observations measured with the other systems (VandenBoer et al., 2014). Therefore, it is feasible to measure HONO using this instrument.

S3. Detailed description of the NO₂、SO₂ and carbon analyzer.

The NO$_2$ analyzer utilized the chemiluminescence technique to measure the concentration of NO$_2$ in the air. This involved converting NO$_2$ to NO using a molybdenum converter, and then quantifying the NO concentration. The principle behind the SO$_2$ analyzer involved measuring the amount of ultraviolet light emitted during the decay of high-energy state SO$_2$. This emitted light was used to calculate the concentration of SO$_2$.

The carbon analyzer principle is primarily based on the NIOSH-5040 method, which involves analyzing the thermal optical transmittance of quartz filter samples. It employs a calibrated non-dispersive infrared sensor to detect the evolving carbon. Under controlled conditions with inert helium gas, carbon formed during a gradually increasing temperature gradient is referred to as OC, while carbon evolved under a mixture of 90% helium.

S4. Sources of HONO

4.1 Direct emission

HONO can be released directly into the atmosphere through vehicle exhaust (Burling et al., 2010;Veres et al., 2010). The lifetime of HONO in the atmosphere is relatively short, so vehicle emissions significantly contribute to urban atmospheric HONO (Chen et al., 2023;Liu et al., 2021a). Considering that there has been a

93 significant reduction in vehicle emissions in urban areas during DC. Additionally, the

94 R-PY site is far from roads. Thus, vehicle emissions may not be the primary source of

95 HONO for the U-ZK site during DC and R-PY sites during entire periods. To further

96 validate the above conclusions, the conditional bivariate probability function diagrams

97 of NO_2 at U-ZK and R-PY sites during PC and DC are depicted in Figure S2. NO_2

98 predominantly originated from long-distance transport at the U-ZK site during DC and

99 the R-PY site during both PC and DC. Consequently, vehicle emissions are only

100 calculated for the U-ZK site during the PC.

101 Here we use the HONO/NO_x ratio to estimate HONO concentration, which is

102 generally considered to be the vehicle emission factor (Kramer et al., 2020;Hao et al.,

103 2020;Yu et al., 2022) for HONO. The calculation formula is as follows：

104 $$[HONO_{emi}] = 0.8\% \times [NO_x] \tag{S1}$$

105 where [$HONO_{emi}$] and [NO_x] represent the HONO concentration emitted by vehicles

106 and the observed NO_x concentration, respectively. Regarding previous studies (Table

107 S3), 0.8% was selected as the vehicle emission factor, considering differences in vehicle

108 type, fuel composition, and other factors (Kramer et al., 2020;Hao et al., 2020;Huang

109 et al., 2017).

110 4.2 Homogeneous reaction of NO and •OH

111 The reaction between NO and •OH is the primary gas-phase reaction source of

112 HONO at high NO concentrations, and the production rate contribution (P_{OH+NO}) for this

113   reaction can be calculated as:

$$P_{OH+NO} = k_{OH+NO}[OH][NO] \tag{S2}$$

115   where k_{OH+NO} (7.2×10^{-12} cm^3 molecule^{-1} s^{-1}) is the rate constant for the reactions at

116   298K (Li et al., 2012). •OH concentration was simulated according to the empirical

117   model (Hu et al., 2022;Wang et al., 2025):

$$[OH] = 4.1 \times 10^9 \times \frac{J(O^1D) \times J(NO_2) \times (140 \times [NO_2]+1) + [HONO] \times J(HONO)}{0.41 \times [NO_2]^2 + 1.7 \times [NO_2] + 1 + [NO] \times k_{NO+OH} + [HONO] \times k_{NO+OH}} \tag{S3}$$

119   where, J (O^1 D), J (NO$_2$), and J (HONO) are the photolysis rates calculated using the

120   TUV model (v5.2; available at http://cprm.acom.ucar.edu/Models/TUV/). The cloud

121   optical depth value for the TUV model was adjusted so that the predicted UVB radiation

122   intensity matched the observations (Lyu et al., 2019;Wang et al., 2022). The calculated

123   •OH concentration varied from 0.1×10^6 to 4×10^6 molecule/cm^3 at U-ZK and 0.1 ×

124   10^6 to 5×10^6 molecule/cm^3 t R-PY, which was comparable to the levels in other cities

125   of North China (Li et al., 2018;Fuchs et al., 2017;Yang et al., 2017). Since there is no

126   photolysis at night, the •OH concentration was assumed to be 0.8×10^6 molecule/cm^3

127   (Wang et al., 2022).

128   4.3 Heterogeneous conversion of NO$_2$ to HONO

129   4.3.1 Heterogeneous dark reactions

130   The heterogeneous conversion of NO$_2$ to HONO on the ground (P$_{ground}$) and on the

131   aerosol surface (P$_{aerosol}$) was calculated based on parameters obtained from experiments

132   or observations.

133
$$P_{ground} = \frac{1}{8}\gamma_1 \times [NO_2] \times C_{NO_2} \times \frac{S_g}{V} \qquad (S4)$$

134
$$P_{aerosol} = \frac{1}{4}\gamma_2 \times [NO_2] \times C_{NO_2} \times \frac{S_a}{V} \qquad (S5)$$

135
$$\frac{S_g}{V} = \frac{1}{MLH} \qquad (S6)$$

136
$$C_{NO_2} = \sqrt{\frac{8RT}{\pi M}} \qquad (S7)$$

137 where C_{NO_2} is the average molecular velocity of NO_2 molecule (m s^{-1}); R is the ideal

138 gas constant; T is the temperature (K); M is the molecular weight of NO_2 (kg mol^{-1});

139 MLH is the height of the mixed layer, which is determined to be 50 m due to HONO

140 formation on the ground level and its short lifetime (Liu et al., 2020a); S_a/V is the

141 surface area to volume ratio of aerosol, estimated by Su et al. (2008).

142 4.3.2 Heterogeneous photo-enhanced reactions

143 The heterogeneous photo-enhanced reactions of NO_2 on the surface of the ground

144 ($P_{ground + hv}$) and the surface of the aerosol ($P_{aerosol + hv}$) were calculated following (Zhang

145 et al., 2020a):

146
$$P_{ground+hv} = \frac{1}{8} \times C_{NO_2} \times \frac{1}{MLH} \times \gamma_1 \times \frac{J_{NO_2}}{J_{NO_2,noon}} \times [NO_2] \qquad (S8)$$

147
$$P_{aerosol+hv} = \frac{1}{4} \times C_{NO_2} \times \frac{S_a}{V} \times \gamma_2 \times \frac{J_{NO_2}}{J_{NO_2,noon}} \times [NO_2] \qquad (S9)$$

148 where J_{NO_2} and $J_{NO_2, noon}$ are the photolysis rate of NO_2 and the photolysis rate of NO_2

149 at noon during the day, respectively.

150 γ_1 and γ_2 are the absorption coefficient of NO_2 on the ground and aerosol surface,

151 respectively, which is assumed to be 4×10^{-6} (Yu et al., 2022;Zhang et al., 2021;Zhang

152 et al., 2020a). Moreover, we discuss the uncertainties based on the recommended values

153 of 2×10^{-6}–1×10^{-5} as upper and lower bounds(Chen et al., 2023;VandenBoer et al.,

154 2013;Wong et al., 2011). Results show (Figure S3) that the uncertainties for P_{ground},

155 $P_{aerosol}$, $P_{groung+hv}$, and $P_{aerosol+hv}$ are −50% to 150%, −50% to 151%, −20% to 120%, and

156 −50% to 121% at the U-ZK, respectively. At the R-PY, the uncertainties for P_{ground},

157 $P_{aerosol}$, $P_{groung+hv}$, and $P_{aerosol+hv}$ are −50% to 150%, −50% to 151%, −20% to 120%, and

158 −20% to 121%, respectively.

159 4.4 Nitrate photolysis

160 The nitrate photolysis ($P_{nitrate}$) was calculated based on the measured nitrate

161 concentration (NO_3^-) from $PM_{2.5}$ and nitrate photolysis rate ($J_{nitrate \rightarrow HONO}$):

162 $$P_{nitrate} = J_{nitrate \rightarrow HONO} \times [NO_3^-] \tag{S10}$$

163 where the $J_{nitrate \rightarrow HONO}$ was simulated by normalizing UV values, when the Zenit Angle

164 is 0°, $J_{nitrate \rightarrow HONO}$ varied within the range of 1.22×10^{-5} to 4.84×10^{-4} s^{-1}, with an average

165 value of 8.24×10^{-5} s^{-1} (Bao et al., 2018).

166 4.5 Soil emissions

167 The emission of HONO from soil is an important source, but the rate is low at lower

168 temperatures. Zhang et al.(2023) suggests that when the atmospheric temperature is

169 below 10℃, the contribution of soil emission to HONO can be disregarded.

170 Furthermore, calculation results from Liu et al.(2020b), Zhang et al.(2023), and

171   others(Liu et al., 2020a) in the North China Plain during winter all indicate that soil

172   emissions only contribute 1% to HONO. During the observation period of U-ZK and

173   R-PY sites, the average temperatures of PC and DC were 4°C and 7 °C, and -1°C and

174   4 °C, respectively. Therefore, it is likely that soil HONO emissions have a minimal

175   impact. Additionally, using a formula to calculate the change in [HONO]* (defined

176   below)(Su et al., 2011) from 3°C to 7°C at U-ZK site in PC and DC is 0.4 ppb, which

177   yields a negligible value. Hence, this study does not take it into consideration.

178

$$[HONO]* = \frac{[H^+]\cdot[NO_2^-]}{K_{a.HNO_2}\cdot H_{HONO}} = \frac{[HNO_2]+[NO_2^-]}{(1+K_{a.HNO_2}/[H^+])H_{HONO}} = \frac{[N(III)]}{(1+K_{a.HNO_2}/[H^+])H_{HONO}}$$

179

180   (S11)

181   where [N(III)] is the total nitrite concentration (HNO_2 + NO_2^-), [H^+] is determined by

182   the soil acidity (pH value), $K_{a.HNO2}$ is the acid dissociation constant and H_{HONO} is the

183   Henry's law coefficient of nitrous acid. Both $K_{a.HNO2}$ and H_{HONO} are functions of

184   temperature:

$$K_{a.HNO_2}(T) = K_{a.HNO_2}(298K)\exp\left(\frac{\Delta H_{a.HNO_2}}{R}\left(\frac{1}{298}-\frac{1}{T}\right)\right)$$

185   (S12)

$$H_{HONO}(T) = H_{HONO}(298K)\exp\left(\frac{\Delta H_{HONO}}{R}\left(\frac{1}{298}-\frac{1}{T}\right)\right)$$

186   (S13)

187   The total nitrite concentration in the aqueous phase of soil, [N(III)], is given by the

188   following equation:

$$[N(III)] = \frac{\rho_w C_{N(III)}}{\theta_g M_N}$$

189   (S14)

190	where ρ_w is the density of water, θ_g is the gravimetric soil water content (mass of soil

191	water / mass of oven-dry soil), $M_N = 0.014$ kg / mol is the molar mass of nitrogen, and

192	$C_{N(III)}$ is the total nitrite (NO_2^- + HNO_2) content of soil expressed as a mass fraction of

193	nitrogen in oven-dry soil (kg / kg). Note that in this study the mass of nitrite or nitrous

194	acid is generally expressed in terms of nitrogen mass (not total molecular mass). The θ_g

195	for most natural soils varies between ~ 0 - 0.4 kg / kg.

196

S5. Estimation of HONO formation rate

198	The redox reaction of NO_2 with SO_2 (R_1) is considered a crucial potential source of

199	high concentrations of HONO in Northern China (Wang et al., 2016b;Cheng, 2016):

200	$$S(IV) + 2NO_2 + H_2O \rightarrow S(IV) + 2H^+ + 2NO_2^- \tag{R_1}$$
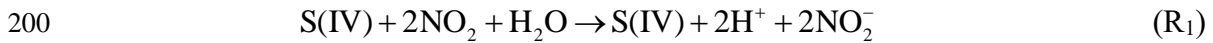
201	The rate expression for the reaction was estimated to:

202	$$d[S(VI)]/dt = k_1[NO_2][S(VI)], \tag{S15}$$

203	where the $k_1 = (1.4 \times 10^5 + 1.24 \times 10^7)/2$ $M^{-1}s^{-1}$ for the pH range < 5;

204	$k_1 = (23.25 \times (pH–5) + 1.4 + 124)/2 \times 10^5$ $M^{-1}s^{-1}$ for the pH range 5 < pH < 5.3;

205	$k_1 = (23.25 \times (pH–5) + 1.4 + 12.6 \times (pH–5.3) + 124)/2 \times 10^5$ $M^{-1}s^{-1}$ for the pH range 5.3 <

206	pH < 5.8;

207	$k_1 = (12.6 \times (pH–5.3) + 124+20)/2 \times 10^5$ $M^{-1}s^{-1}$ for the pH range 5.8 < pH < 8.7;

208	and $k_1 = (2 \times 10^6 + 1.67 \times 10^7)/2$ $M^{-1}s^{-1}$ for the pH range pH > 8.7. (Seinfeld et al., 1998)

209	In the above calculation formulas, the concentration of gas in the liquid is determined

210   by Henry's constant (H^*). The calculation formula is in Table S4. SO_2 has a dissociation

211   equilibrium in the solution, producing HSO_3^- and SO_3^{2-}. The ionization constants (K)

212   are shown in the following Table S5. The H* and K are temperature-dependent. The

213   values are given in Tables S4 and S5 under the condition of 298K, converted to the

214   value under the actual temperature using the following calculation formula:

215    $$H(T) \text{ or } K(T) = H(T_{298K}) \text{ or } K(T_{298K}) \exp\left[-\frac{\Delta H_{298K}}{R}\left(\frac{1}{T} - \frac{1}{298K}\right)\right] \qquad (S16)$$

216   where $H(T)$、$K(T)$、$H(T_{298K})$, and $K(T_{298K})$ represent the H* and K at actual temperature

217   and 298 K, respectively.

218   Influences of ionic strength on R_1 were not considered because of the high values

219   predicted by the ISORROPIA-II model during the sampling periods (Cheng et al.,

220   2016). To evaluate the effects of mass transport, the formulation of a standard resistance

221   model was adopted:

222    $$\frac{1}{R_{H,aq}} = \frac{1}{R_{aq}} + \frac{1}{J_{aq,lim}} \qquad (S17)$$

223   where $R_{H, aq}$ is the sulfate production rate, R_{aq} is the aqueous-phase reaction rate and

224    $J_{aq,lim}$ is the limiting mass transfer rate. which could be calculated by the formulas as

225   follows:

226    $$J_{aq,lim} = \min\{J_{aq}(SO_2), J_{aq}(X)\} \qquad (S18)$$

227    $$J_{aq}(X) = k_{MT}(X) \cdot [X] \qquad (S19)$$

228   where [X] refers to the aqueous-phase concentrations of SO_2 or the oxidants O_{xi}

229   calculated by the equation in Table S4. The mass transfer rate coefficient $k_{MT}(X)$ (s^{-1})

230   can be calculated by:

231
$$k_{MT} = [\frac{R_p^2}{3D_g} + \frac{4R_p}{3\alpha v}]^{-1}$$
(S20)

232   where R_p is the aerosol radius, D_g is the gas-phase molecular diffusion coefficient (0.2

233   cm^2 s^{-1} at 293K), v is the mean molecular speed of X (3×10^4 cm s^{-1}), and a is the mass

234   accommodation of X on the droplet surface, and we adopted values of 0.11 and $2E^{-4}$ for

235   SO_2 and NO_2, respectively referring to Cheng et al. (2016).
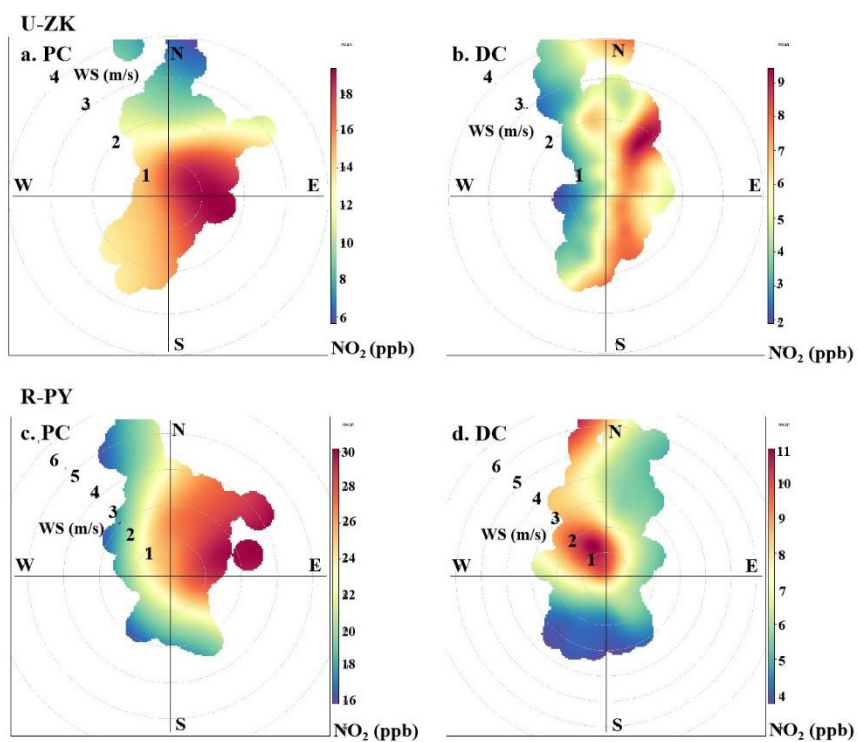
236 **Figures**
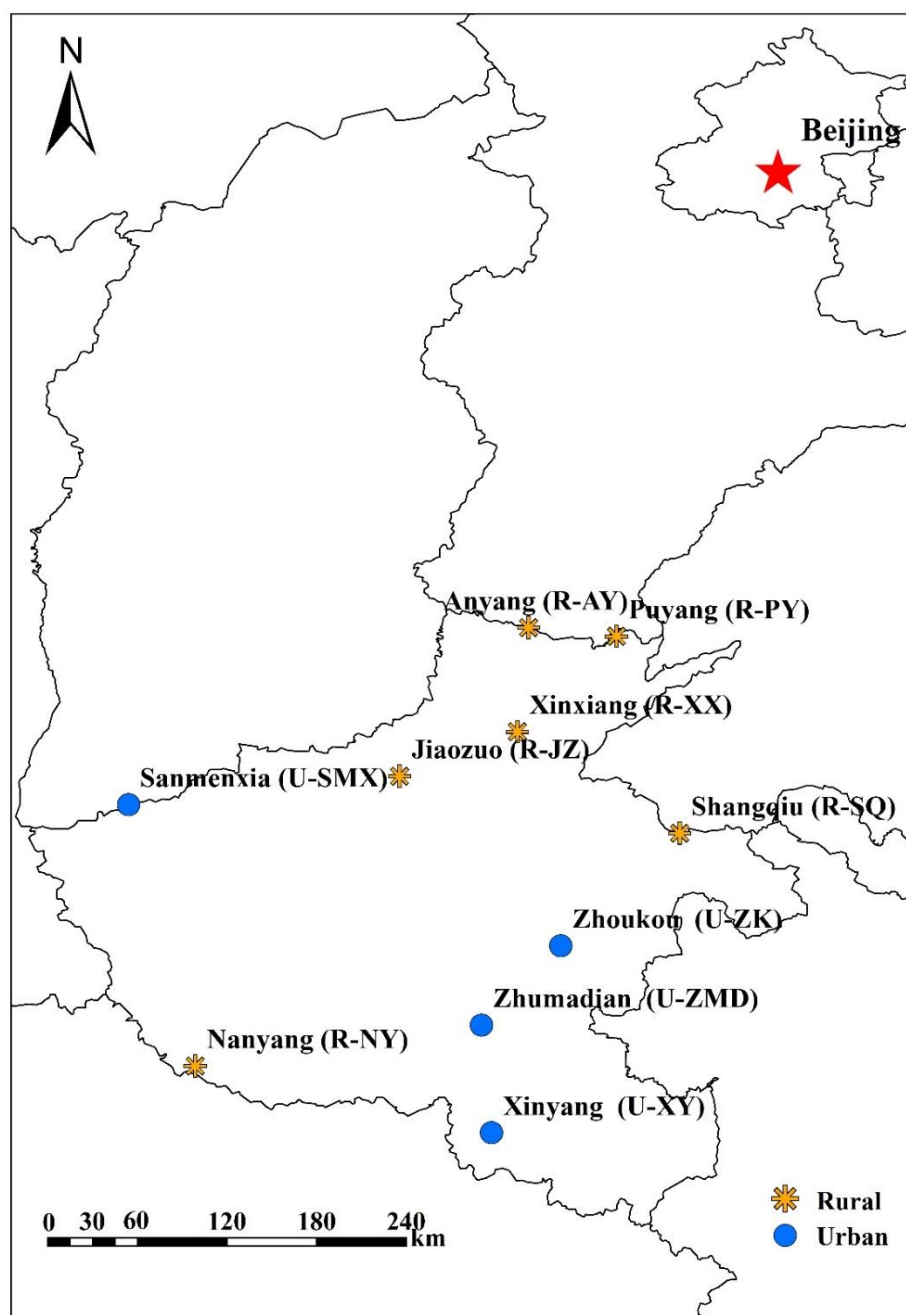
237

238 Figure S1. Sampling point map in Henan Province, China. © 2019 National Geomatics

239 Center of China. i.e., urban sites at Sanmenxia (U-SMX), Zhoukou (U-ZK), Zhuamdian

240 (U-ZMD) and Xinyang (U-XY), rural sites at Anyang (R-AY), Xinxiang (R-XX),

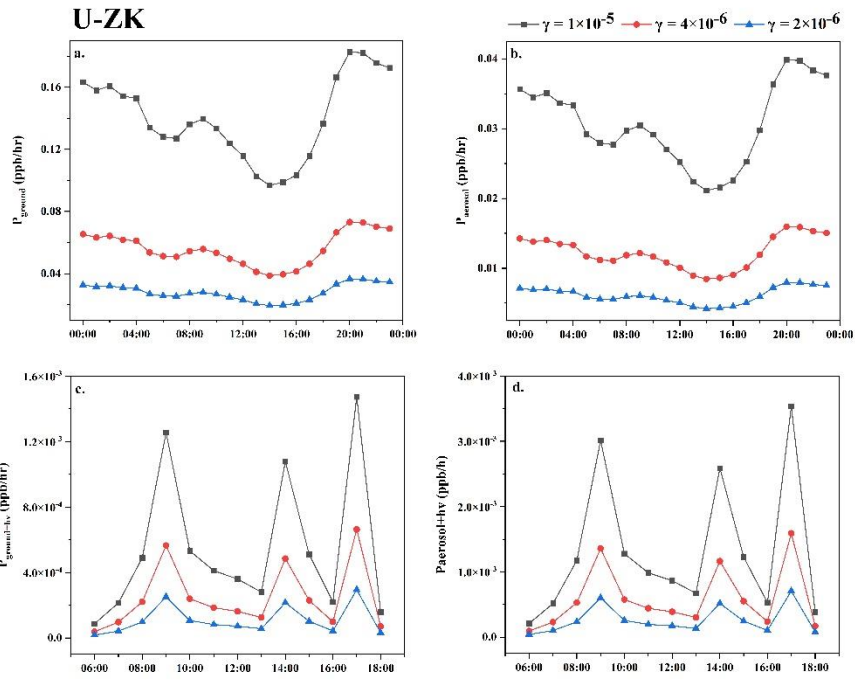241 Puyang (R-PY), Jiaozuo(R-JZ), Shangqiu (R-SQ) and Nanyang (R-NY). All rights
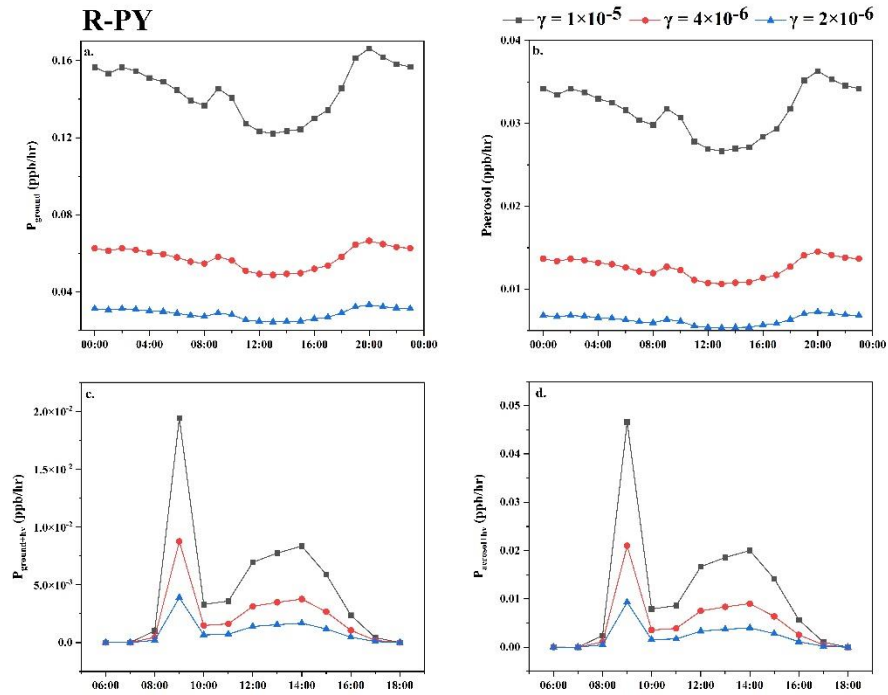
242 reserved.

14

243

244

Figure S2. Result of conditional bivariate probability function plots: NO_2 at U-ZK and R-PY sites before (PC) and during (DC) the COVID-19 outbreak. The color scale bar represents NO_2 concentration.

248

249

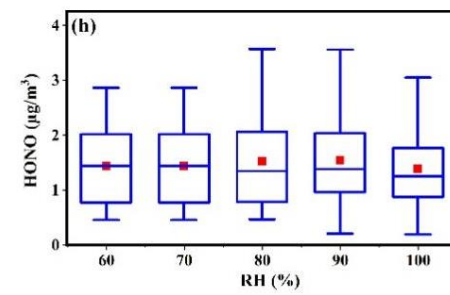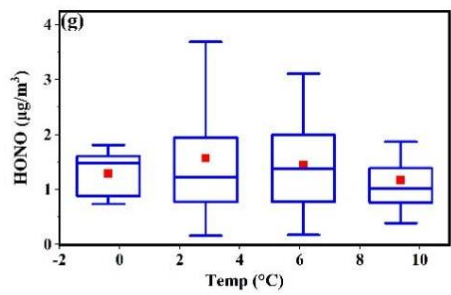Figure S3. HONO production rate using different uptake rates of NO_2 at the U-ZK and R-PY sites before (PC) and during (DC) the COVID-19 outbreak. (a)P_{ground}, (b) $P_{aerosol}$, (c) $P_{ground+hv}$, and (d) $P_{aerosol+hv}$

253

a.U-ZK

254

b.R-PY
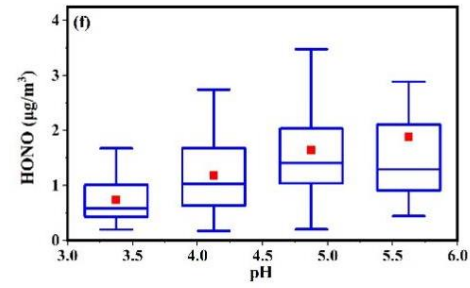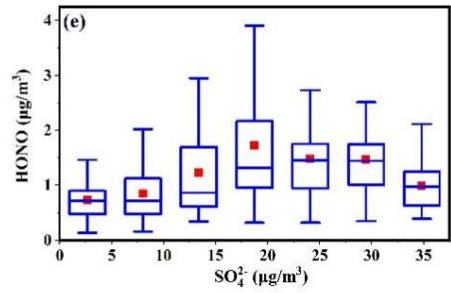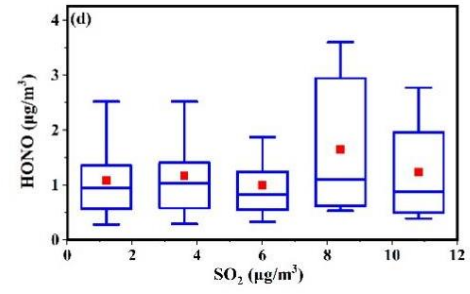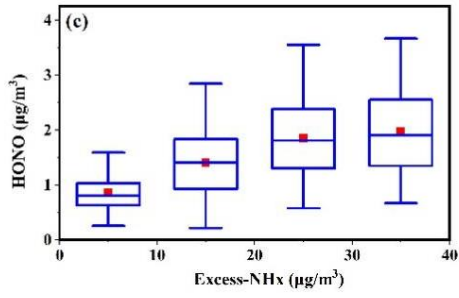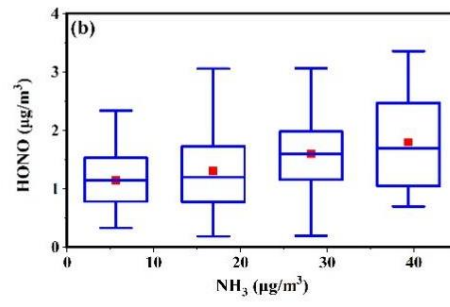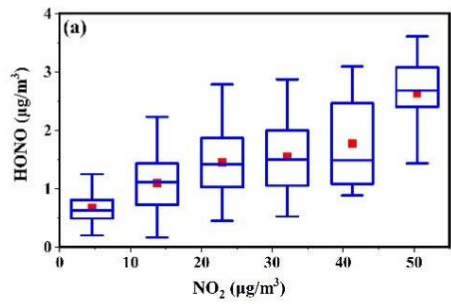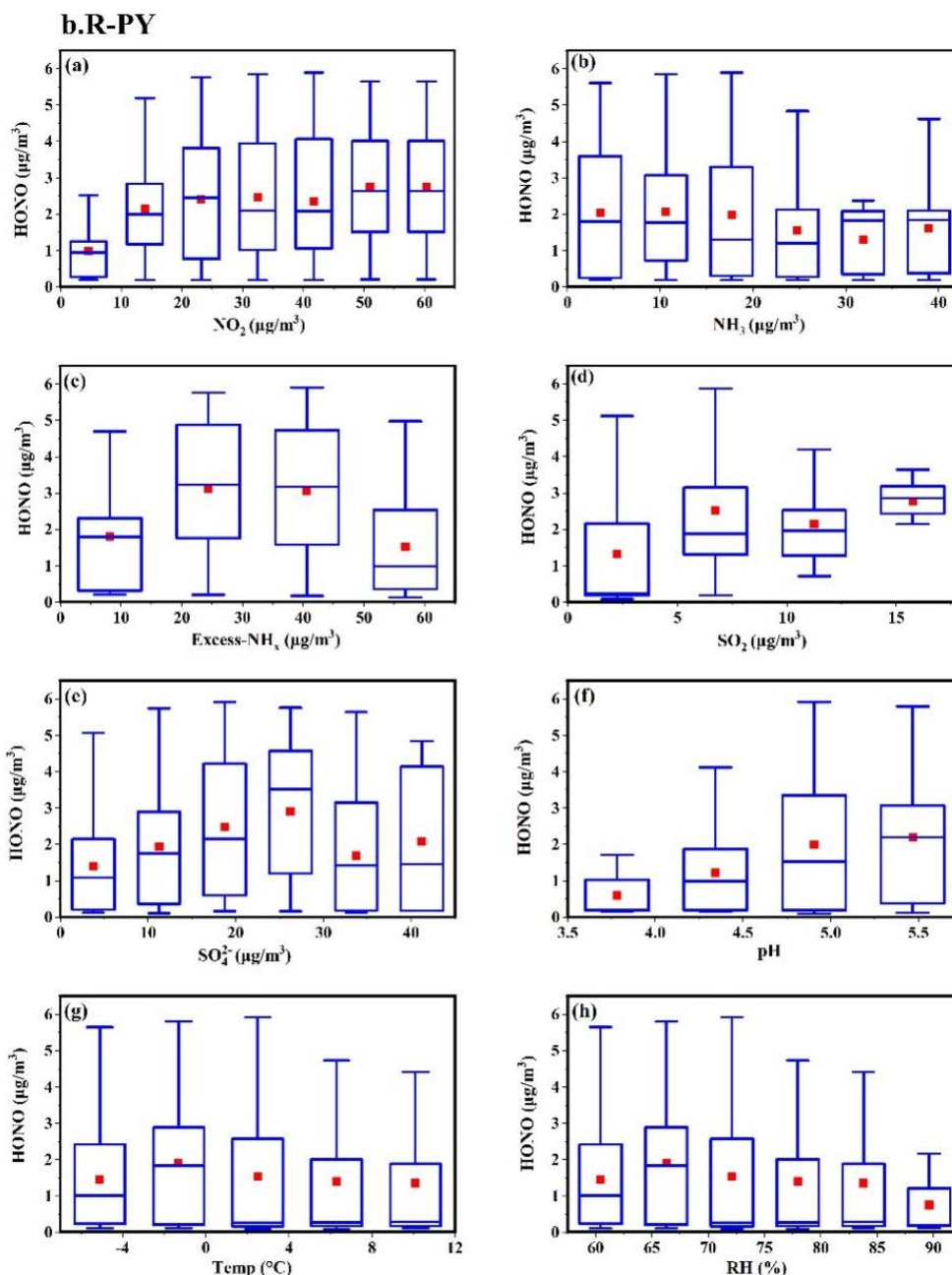
Figure S4. Relationship between HONO and main influencing factors during (DC) the COVID-19 outbreak at U-ZK and R-PY sites. In each box, the top, middle, and bottom lines represent the 75, 50, and 25 percentiles of statistical data, respectively; the upper and lower whiskers represent the 90 and 10 percentiles of statistical data, respectively.

262

263
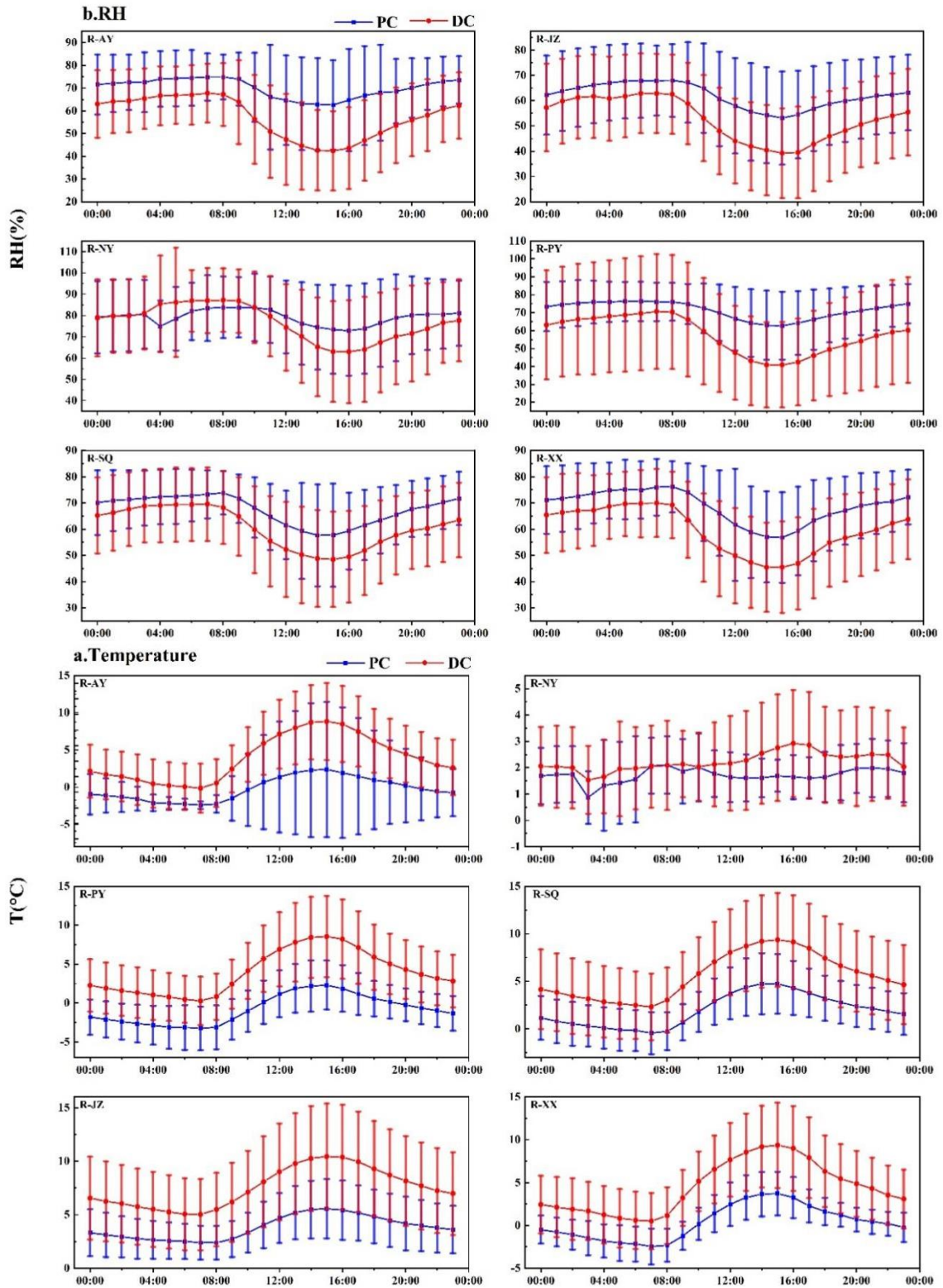
264　　Figure S5. Daily changes in temperature and relative humidity (RH) in rural sites

265　　before (PC) and during (DC) the COVID-19 outbreak, the error bar represents the

266　　standard deviation. The upper and lower whiskers represent the standard deviation.
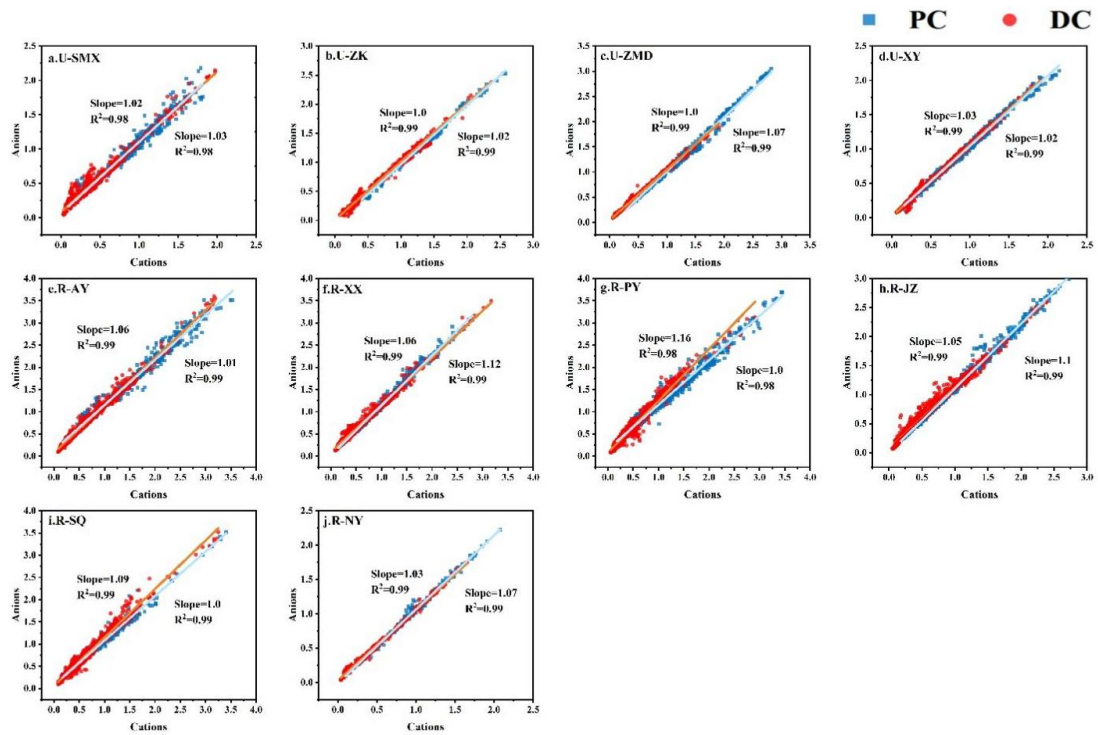
Figure S6. The equilibrium state of anions and cations at ten sites before (PC) and during (DC) the COVID-19 outbreak.
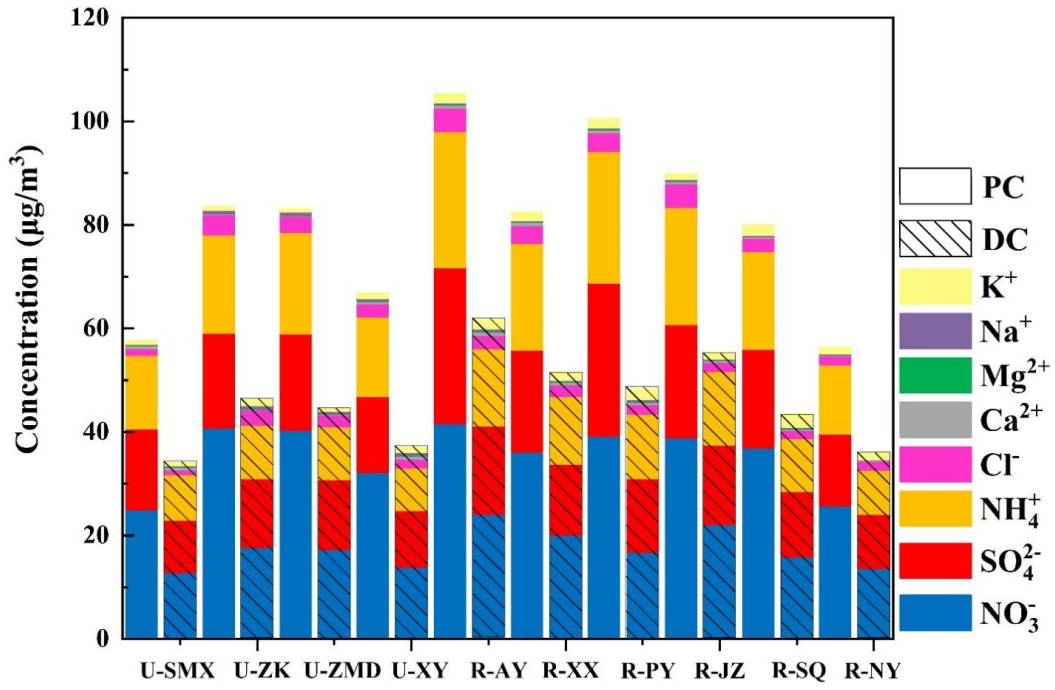
270

271 Figure S7. Concentrations of the water-soluble ions at the ten sites before (PC) and

272 during (DC) the COVID-19 outbreak.

273

274
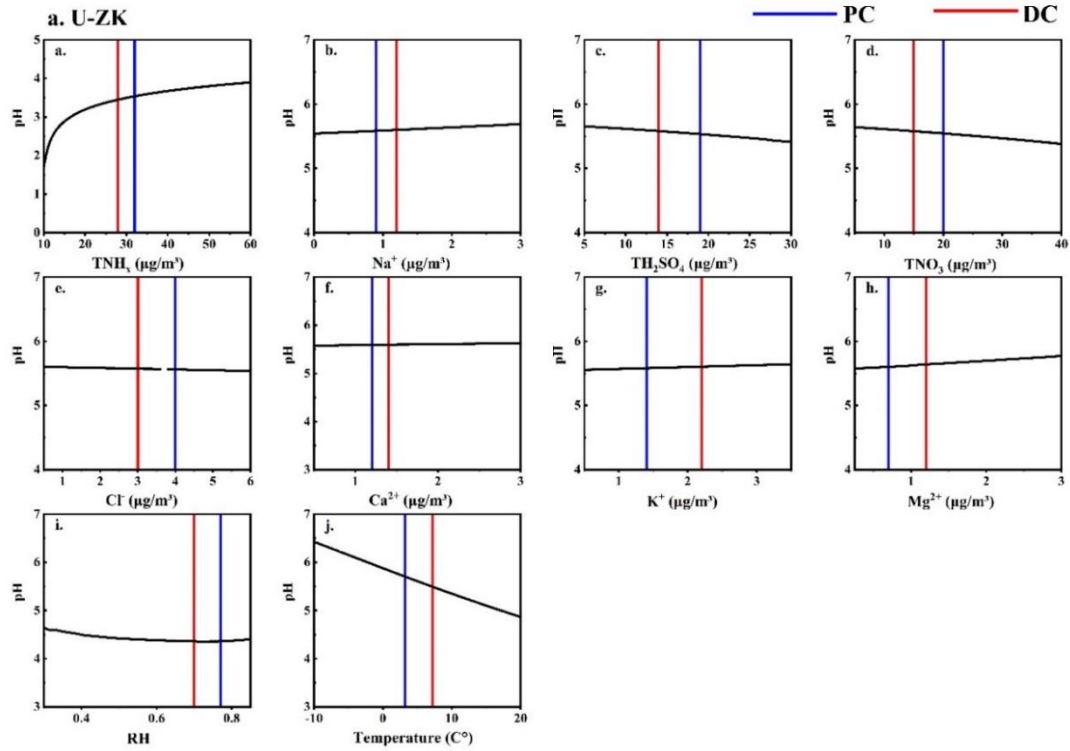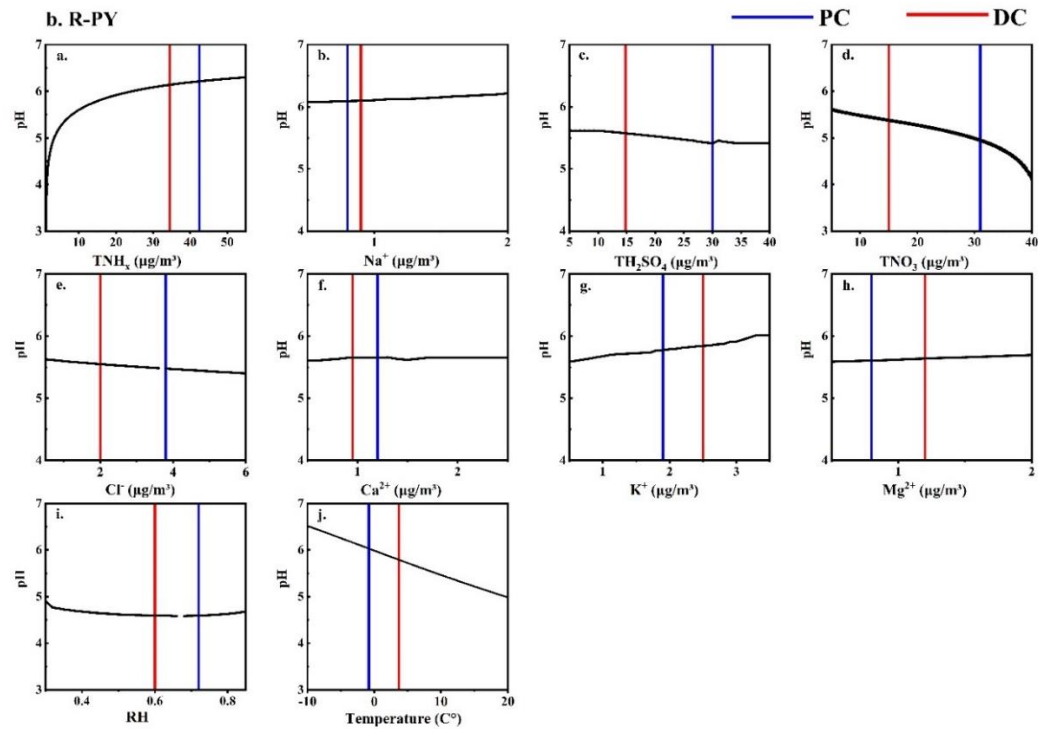
Figure S8. Sensitivity tests of pH to each factor. The vertical bar represents the mean values before (PC) and during (DC) the COVID-19 outbreak. A given range for a variable (i.e., TNH_x) with corresponding average values of other parameters (i.e., TH_2SO_4, TNO_3, TCl, TNa, K^+, Ca^{2+}, Mg^{2+}, T, and RH) was simulated to compare its effects on pH.
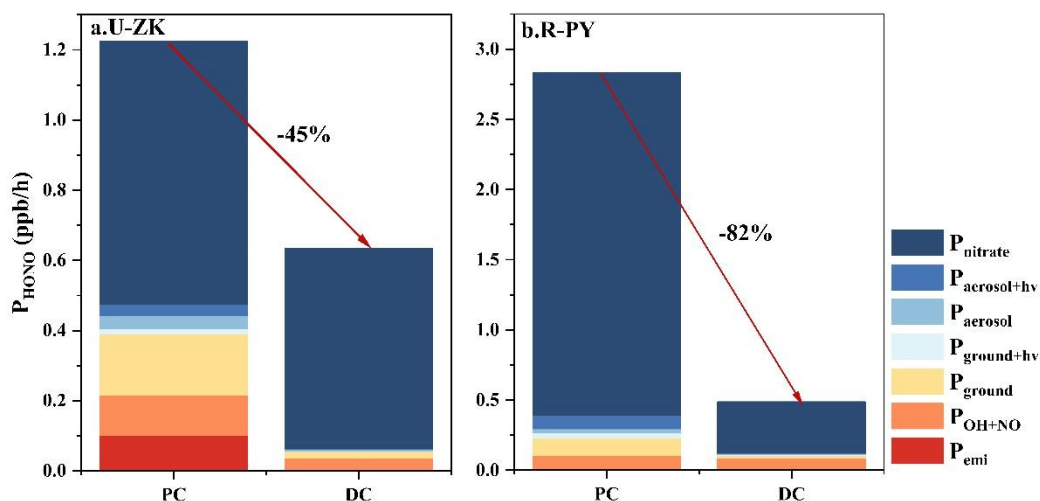
Figure S9. Maximum uncertainty values for HONO sources at U-ZK and R-PY sites were compared between the pre-COVID-19 outbreak (PC) and (DC) periods. Refer to Text S4 for details on the calculation methods.
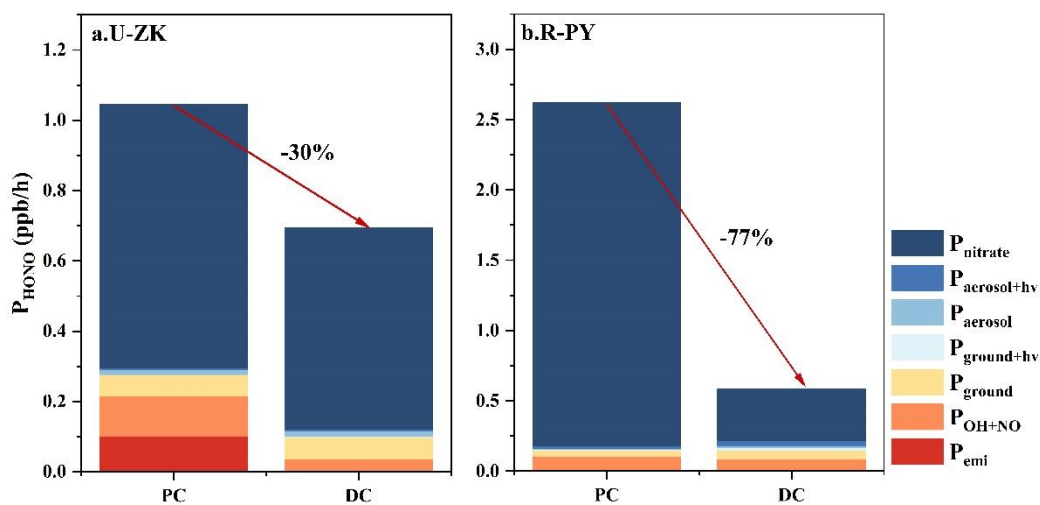
Figure S10. Minimum uncertainty values for HONO sources at U-ZK and R-PY sites were compared between the pre-COVID-19 outbreak (PC) and (DC) periods. Refer to Text S4 for details on the calculation methods.

291
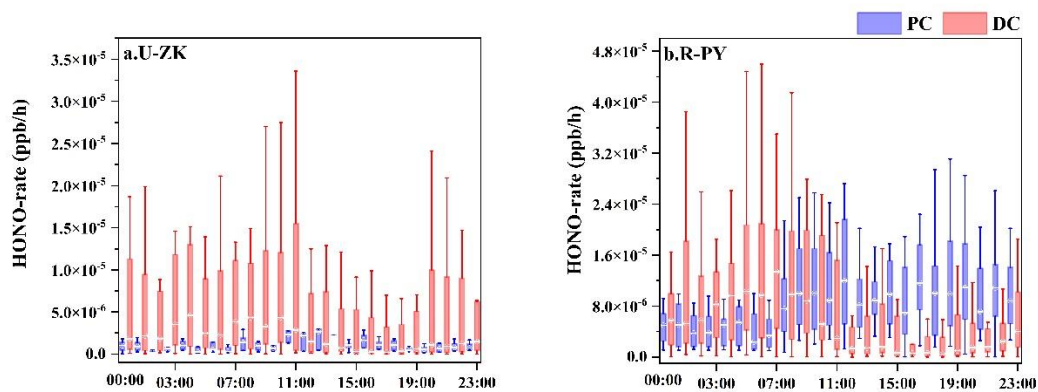
Figure. S11. HONO production rate through R_1 at U-ZK and R-PY sites before (PC)

and during (DC) the COVID-19 outbreak. In each box, the top, middle, and bottom

lines represent the 75, 50, and 25 percentiles of statistical data, respectively; the upper

and lower whiskers represent the 90 and 10 percentiles of statistical data, respectively.

296

297

298

299
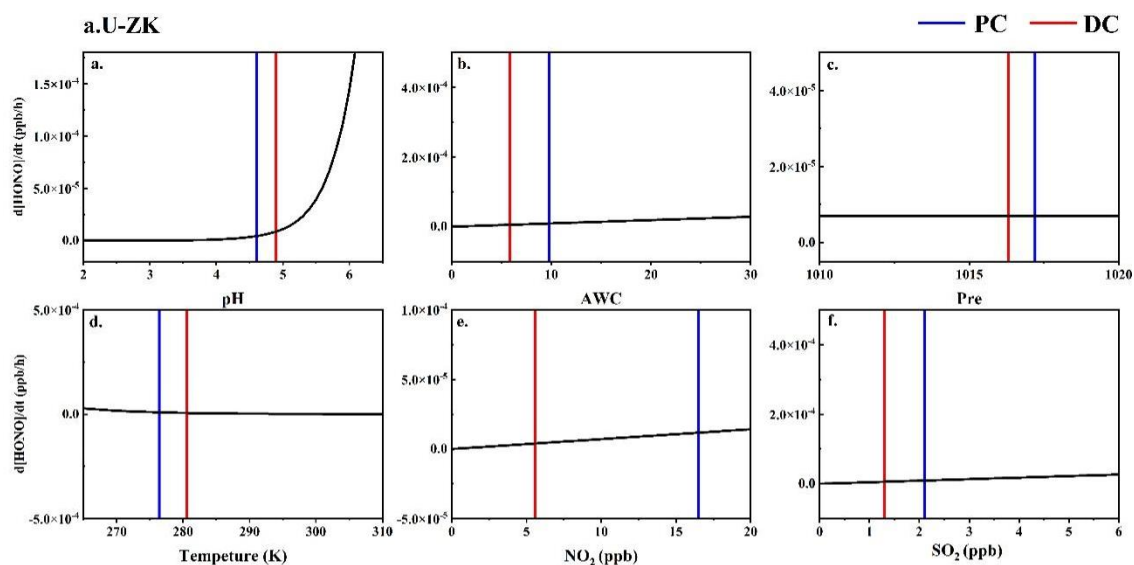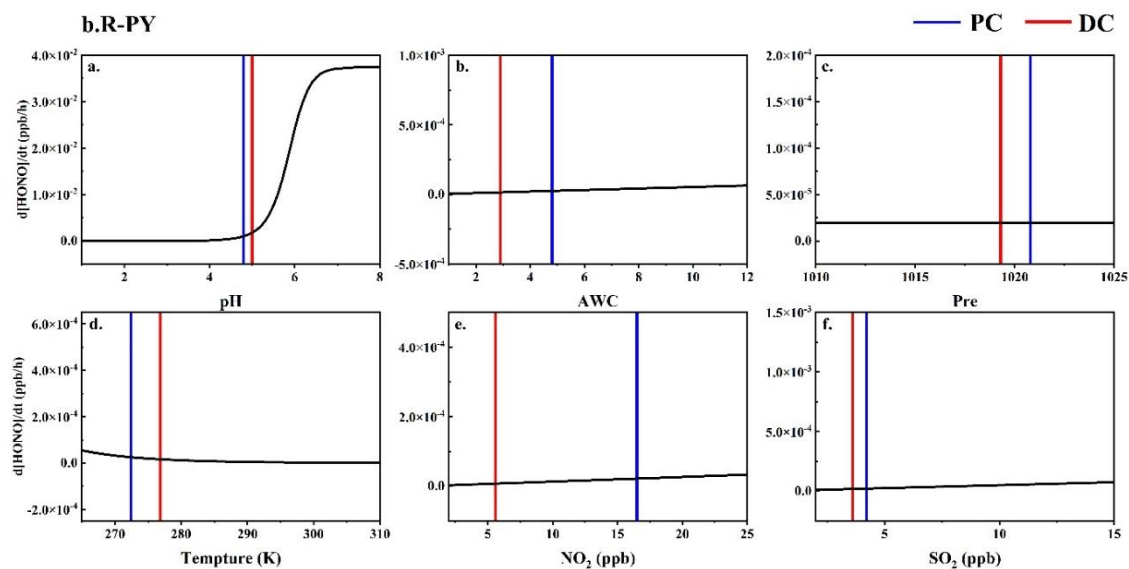
Figure S12. Sensitivity of HONO product rate to each factor. The vertical bar represents the mean values before (PC) and during (DC) the COVID-19 outbreak. The real-time measured values of a variable and the average values of other parameters were input into the production rate of the R_1 reaction.

304
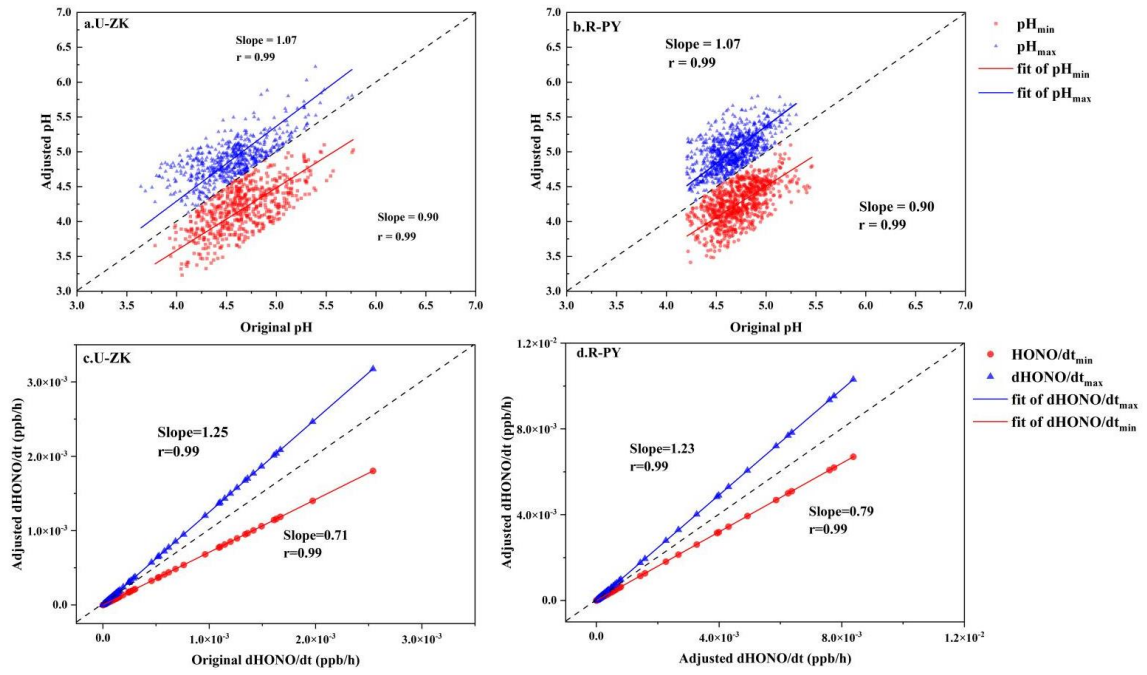
Figure S13. pH and R_1 uncertainties at the U-ZK and R-PY sites are based on two

extreme scenarios of sensitivity to measurement uncertainty.

307

308

309

310

Tables

Table S1. Descriptions of the ten sampling sites in Henan Province, China.

Observation sites	Classifications	Abbreviations	Coordinates	Locations	Surrounding environment
Sanmenxia	Urban site	U-SMX	34.79 °N, 111.16 °E	Sanmenxia Environmental Protection Bureau	Roads, residential areas
Zhoukou	Urban site	U-ZK	33.65° N, 114.65° E	Chuanhui District People's Government	Roads, residential areas
Zhumadian	Urban site	U-ZMD	33.01° N, 114.01° E	Huanghuai College	Roads, residential areas, shopping malls
Xinyang	Urban site	U-XY	32.14° N, 114.09° E	Xinyang Museum	Roads, residential areas, shopping malls
Anyang	Rural site	R-AY	36.22°N, 114.39° E	Baizhuang Town Xindian North Street China Resources Gas (Andan Station)	Highways, villages, farmland
Xinxiang	Rural site	R-XX	35.38° N, 114.30° E	Banzao Township Central School in Yanjin County	Villages, farmland
Puyang	Rural site	R-PY	36.15° N, 115.10° E	Nanle County Longwang Temple Station	Villages, farmland
Jiaozuo	Rural site	R-JZ	35.02° N, 113.35° E	The Second River Bureau of Jiefeng Village, Beiguo Township, Wuxi County	Villages, farmland
Shangqiu	Rural site	R-SQ	34.56° N, 115.61° E	Liangyuan Huanghe Gudao National Forest Park	Highways, villages, farmland
Nanyang	Rural site	R-NY	32.68° N, 111.70° E	Nanyang Tangshan Park	Villages, farmland

Table S2. The value of ρ_s in other studies.

Observation site	Period	ρ_s (g/cm^3)	Reference
Beijing	Dec 2016	1.4	(Liu et al., 2017)
Tianjin	Dec-Jun 2015	1.3	(Shi et al., 2017)
Xi'an	Nov-Dec 2012	1.4	(Guo et al., 2017)
Hohhot	Winter 2015	1.35	(Wang et al., 2019)
Northeastern USA	Feb-Mar 2015	1.4	(Guo et al., 2016)
Crete, Greece	Aug-Nov 2012	1.35	(Bougiatioti et al., 2016)
Alabama, USA	Jun-Jul 2013	1.4	(Guo et al., 2015)
Georgia, USA	Aug-Oct 2016	1.4	(Nah et al., 2018)

Table S3. Summary of vehicle emission factors.

Observation site	Period	Emission factor (%)	Reference
Beijing	2020	0.79	(Meng et al., 2020)
Hong Kong	2015	0.4–1.8	(Yun et al., 2017)
Hong Kong	2011	0.5–1.6	(Xu et al., 2015)
Kiesberg Tunnel	2001	0.8	(Kleffmann et al., 2003)
Kiesberg Tunnel	1997	0.3–0.8	(Kurtenbach and Wiesen, 2001)
Guangzhou	2019	1.31	(Li et al., 2021)

Table S4. Constants for calculating the apparent Henry's constant (H*).

Equilibrium	H (M atm^{-1}) at 298K	$-\triangle H_{298K}/R$ (K)
$SO_2(g) \leftrightarrow SO_2(aq)$	1.23	3145.3
$NO_2(g) \leftrightarrow NO_2(aq)$	1.00E-02	2516.2

Table S5. Constants for calculating the ionization constants (K).

Equilibrium	K (M) at 298K	$-\triangle H_{298K}/R$ (K)
$SO_2 \cdot H_2O \leftrightarrow H^+ + HSO_3^-$	1.30E-02	1960
$HSO_3^- \leftrightarrow H^+ + SO_3^{2-}$	6.60E-08	1500

325   Table S6. Comparisons of NH_3 concentrations (mean ± standard deviation) (μg/m^3)

326   from studies in other cities.

Sampling sites	Seasons	Years	NH_3 (μg/m^3)	Sites	References
Delhi, India	Winter	2013–2015	19.2 ± 3.5	Urban	(Saraswati et al., 2019)
Osaka, Japan	Winter	2015	1.5 ± 0.7	Urban	(Huy et al., 2017)
Toronto, Canada	Winter	2007	0.8 ± 0.5	Urban	(Hu et al., 2014)
Kanpur, India	Winter	2007	21.7 ± 5.8	Urban	(Behera and Sharma, 2010)
Nanjing	Winter	2014	6.7	Urban	(Wang et al., 2016b)
Yangtze River Delta	Winter	2019	9.3 ± 4.0	Urban	(Wang et al., 2021)
Shanghai	Winter	2014	2.8 ± 1.0	Urban	(Wang et al., 2018)
Tianjin	Winter	2015	12.0	Urban	(Shi et al., 2019)
Xi'an	Winter	2012	17.5 ± 9.1	Urban	(Wang et al., 2016a)
Fujian	Winter	2016	12.8 ± 4.8	Urban	(Wu et al., 2017)
Beijing	Winter	2015	15.1 ± 2.9	Urban	(Wang et al., 2016a)
Beijing	Winter	2017	13.1 ± 1.6	Urban	(Zhang et al., 2020b)
Beijing	Winter	2020	19.9 ± 3.8	Urban	(Zhang et al., 2020b)
Taoyuan	Winter	2017–2018	1.7 ± 1.9	Urban	(Duan et al., 2021)
Zhengzhou	Winter	2018	19.0 ± 4.0	Rural	(Wang et al., 2020)
Quzhou	Winter	2019	29.5 ± 2.2	Rural	(Feng et al., 2022)
Gucheng	Winter	2016	9.3	Rural	(Xu et al., 2019)
Chongming	Winter	2019–2020	9.3 ± 4.0	Rural	(Lv et al., 2022)
Shanglan	Winter	2017–2018	2.5 ± 2.6	Rural	(Duan et al., 2021)

327

328

329 Table S7. The concentration (mean ± standard deviation) of relative humidity (RH),
330 temperature (T), $\varepsilon(NH_4^+)$ at the ten sites before (PC) and during (DC) the COVID-19
331 outbreak.

Sites	Substances	Total	PC	DC
U-SMX	RH (%)	54.8 ± 18.0	60.6 ± 16.5	51.2 ± 18.0
	T (°C)	5.6 ± 4.2	3.1 ± 2.1	7.0 ± 4.4
	$\varepsilon(NH_4^+)$	0.43 ± 0.20	0.54 ± 0.18	0.36 ± 0.18
U-ZK	RH (%)	70.1 ± 21.9	73.6 ± 14.5	69.4 ± 22.4
	T (°C)	6.4 ± 4.3	3.8 ± 2.3	7.0 ± 4.5
	$\varepsilon(NH_4^+)$	0.43 ± 0.20	0.59 ± 0.14	0.32 ± 0.17
U-ZMD	RH (%)	74.9 ± 23.3	84.4 ± 17.8	68.9 ± 24.4
	T (°C)	5.6 ± 4.6	2.9 ± 2.7	7.4 ± 4.8
	$\varepsilon(NH_4^+)$	0.48 ± 0.21	0.62 ± 0.17	0.38 ± 0.18
U-XY	RH (%)	77.0 ± 22.1	86.7 ± 13.3	74.3 ± 23.3
	T (°C)	7.7 ± 4.5	4.7 ± 2.2	8.5 ± 4.6
	$\varepsilon(NH_4^+)$	0.55 ± 0.21	0.71 ± 0.14	0.45 ± 0.18
R-AY	RH (%)	62.2 ± 17.9	70.1 ± 14.9	57.2 ± 17.8
	T (°C)	2.6 ± 0.9	-0.2 ± 2.5	4.4 ± 4.7
	$\varepsilon(NH_4^+)$	0.46 ± 0.17	0.57 ± 0.15	0.39 ± 0.14
R-XX	RH (%)	63.0 ± 17.0	68.7 ± 14.6	59.5 ± 17.5
	T (°C)	2.9 ± 4.6	0.3 ± 2.8	4.4 ± 4.8
	$\varepsilon(NH_4^+)$	0.40 ± 0.17	0.52 ± 0.16	0.35 ± 0.14
R-PY	RH (%)	63.6 ± 18.0	71.5 ± 14.6	57.6 ± 18.0
	T (°C)	1.7 ± 4.8	-0.8 ± 3.2	3.6 ± 4.9
	$\varepsilon(NH_4^+)$	0.43 ± 0.17	0.58 ± 0.13	0.34 ± 0.13
R-JZ	RH (%)	56.3 ± 18.5	62.0 ± 16.7	52.8 ± 18.7
	T (°C)	4.1 ± 4.4	1.7 ± 2.6	5.6 ± 4.7
	$\varepsilon(NH_4^+)$	0.37 ± 0.14	0.46 ± 0.13	0.32 ± 0.13
R-SQ	RH (%)	63.2 ± 15.6	67.5 ± 12.6	60.5 ± 17.0
	T (°C)	4.2 ± 4.5	2.0 ± 2.9	5.6 ± 4.7
	$\varepsilon(NH_4^+)$	0.45 ± 0.19	0.63 ± 0.12	0.35 ± 0.14
R-NY	RH (%)	75.9 ± 19.1	79.3 ± 17.7	73.9 ± 19.6
	T (°C)	5.7 ± 3.8	3.6 ± 2.6	6.9 ± 3.9
	$\varepsilon(NH_4^+)$	0.59 ± 0.19	0.73 ± 0.12	0.52 ± 0.18

332

333   Table S8. The concentration (mean ± standard deviation) of required ammonia

334   (Required-NH_x) and excess ammonia (Excess-NH_x) at the ten sites before (PC) and

335   during (DC) the COVID-19 outbreak.

Sites	Substances	Total (μg/m³)	PC (μg/m³)	DC (μg/m³)
U-SMX	Required-NH_4^+	9.1 ± 7.1	12.7 ± 7.1	7.0 ± 6.2
	Excess-NH_4^+	14.7 ± 11.2	13.6 ± 10.4	15.3 ± 11.6
U-ZK	Required-NH_4^+	15.2 ± 9.6	21.4 ± 8.6	11.6 ± 8.4
	Excess-NH_4^+	14.6 ± 8.3	11.9 ± 6.0	16.1 ± 9.0
U-ZMD	Required-NH_4^+	13.9 ± 9.8	19.4 ± 9.8	10.4 ± 8.0
	Excess-NH_4^+	12.8 ± 8.7	11.6 ± 8.2	13.6 ± 8.8
U-XY	Required-NH_4^+	10.2 ± 7.5	14.6 ± 7.3	7.4 ± 6.2
	Excess-NH_4^+	7.8 ± 4.6	6.5 ± 4.4	8.7 ± 4.5
R-AY	Required-NH_4^+	17.1 ± 12.4	23.9 ± 13.4	12.8 ± 9.5
	Excess-NH_4^+	21.2 ± 9.4	20.2 ± 9.2	21.9 ± 9.4
R-XX	Required-NH_4^+	13.5 ± 9.6	18.0 ± 9.8	10.7 ± 8.2
	Excess-NH_4^+	23.3 ± 11.4	19.6 ± 10.8	25.6 ± 11.2
R-PY	Required-NH_4^+	13.8 ± 11.0	22.1 ± 12.5	9.3 ± 6.6
	Excess-NH_4^+	22.3 ± 10.8	17.5 ± 8.6	25.0 ± 11.0
R-JZ	Required-NH_4^+	15.4 ± 10.4	20.3 ± 10.6	12.5 ± 9.1
	Excess-NH_4^+	27.5 ± 12.9	26.0 ± 13.1	28.4 ± 12.7
R-SQ	Required-NH_4^+	13.2 ± 9.1	19.1 ± 8.9	9.9 ± 7.3
	Excess-NH_4^+	15.1 ± 8.6	10.1 ± 5.4	17.9 ± 8.7
R-NY	Required-NH_4^+	9.9 ± 6.6	13.0 ± 6.9	8.1 ± 5.8
	Excess-NH_4^+	6.0 ± 3.6	4.4 ± 3.3	6.9 ± 3.4

336

337 Table S9. Comparison of the particle pH values in this study (PC/DC) and other sites
338 (mean or mean ± standard).

	Sites	Periods	pH	References
Urban	Sanmenxia	Jan–Feb 2020	4.6 ± 0.5/4.8 ± 0.9	This study
	Zhoukou	Jan–Feb 2020	4.6 ± 0.6/5.1 ± 0.4	
	Zhumadian	Jan–Feb 2020	4.6 ± 0.3/4.8 ± 1.2	
	Xinyang	Jan–Feb 2020	4.2 ± 0.3/4.6 ± 1.3	
Rural	Anyang	Jan–Feb 2020	4.5 ± 0.4/4.6 ± 0.8	
	Xinxiang	Jan–Feb 2020	4.8 ± 0.5/4.9 ± 0.9	
	Puyang	Jan–Feb 2020	4.8 ± 0.3/5.1 ± 0.9	
	Jiaozuo	Jan–Feb 2020	4.9 ± 0.5/5.1 ± 0.8	
	Shangqiu	Jan–Feb 2020	4.5 ± 0.3/4.7 ± 0.8	
	Nanyang	Jan–Feb 2020	4.2 ± 0.5/4.4 ± 0.7	
Urban	Beijing	Jan–Feb 2015	4.5	(Guo et al., 2017)
	Beijing	Dec 2016	4.3 ± 0.4	(Liu et al., 2017)
	Beijing	Feb 2017	4.5 ± 0.7	(Ding et al., 2019)
	Tianjin	Dec–Jun 2015	4.9 ± 1.4	(Shi et al., 2017)
	Tianjin	Aug 2015	3.4 ± 0.5	(Shi et al., 2019)
	Hohhot	Winter	5.7	(Wang et al., 2019)
	Mt. Tai	Summer	2.9 ± 0.5	(Liu et al., 2021b)
	Taoyuan	Nov 2017–Jan 2018	5.1 ± 1.0	(Duan et al., 2021)
	Zhengzhou	Jan 2018	4.5	(Wang et al., 2020)
	Anyang	Jan 2018	4.8	(Wang et al., 2020)
Mountain	Mt. Tai	Summer	3.6 ± 0.7	(Liu et al., 2021b)
Rural	Shanglan	Nov 2017–Jan 2018	5.5 ± 1.1	(Duan et al., 2021)

339

References

Behera, S. N., and Sharma, M.: Investigating the potential role of ammonia in ion chemistry of fine particulate matter formation for an urban environment, Sci. Total Environ., 408, 3569–3575, https://doi.org/10.1016/j.scitotenv.2010.04.017, 2010.

Bougiatioti, A., Nikolaou, P., Stavroulas, I., Kouvarakis, G., Weber, R., Nenes, A., Kanakidou, M., and Mihalopoulos, N.: Particle water and pH in the eastern Mediterranean: source variability and implications for nutrient availability, Atmos. Chem. Phys., 16, 4579–4591, https://doi.org/10.5194/acp-16-4579-2016, 2016.

Burling, I. R., Yokelson, R. J., Griffith, D. W. T., Johnson, T. J., Veres, P., Roberts, J. M., Warneke, C., Urbanski, S. P., Reardon, J., Weise, D. R., Hao, W. M., and de Gouw, J.: Laboratory measurements of trace gas emissions from biomass burning of fuel types from the southeastern and southwestern United States, Atmos. Chem. Phys., 10, 11115–11130, https://doi.org/10.5194/acp-10-11115-2010, 2010.

Chen, D., Zhou, L., Liu, S., Lian, C., Wang, W., Liu, H., Li, C., Liu, Y., Luo, L., Xiao, K., Chen, Y., Qiu, Y., Tan, Q., Ge, M., and Yang, F.: Primary sources of HONO vary during the daytime: Insights based on a field campaign, Sci. Total Environ., 903, https://doi.org/10.1016/j.scitotenv.2023.166605, 2023.

Cheng, Y., Zheng, G., Wei, C., Mu, Q., Zheng, B., Wang, Z., Gao, M., Z., Q., He, K., Carmichael, G., Pöschl, U., and Su, and H.: Reactive nitrogen chemistry in aerosol water as a source of sulfate during haze events in China, Sci. Adv., 2, e1601530., https://doi.org/10.1126/sciadv.1601530, 2019.

Ding, J., Zhao, P., Su, J., Dong, Q., Du, X., and Zhang, Y.: Aerosol pH and its driving factors in Beijing, Atmos. Chem. Phys. 19, 7939–7954, https://doi.org/10.5194/acp-19-7939-2019, 2019.

Duan, X., Yan, Y., Peng, L., Xie, K., Hu, D., Li, R., and Wang, C.: Role of ammonia in secondary inorganic aerosols formation at an ammonia-rich city in winter in North China: A

comparative study among industry, urban, and rural sites, Environ. Pollut., 291, 118151, https://doi.org/10.1016/j.envpol.2021.118151, 2021.

Feng, S., Xu, W., Cheng, M., Ma, Y., Wu, L., Kang, J., Wang, K., Tang, A., Collett, J. L., Fang, Y., Goulding, K., Liu, X., and Zhang, F.: Overlooked nonagricultural and wintertime agricultural NH_3 emissions in Quzhou county, North China Plain: evidence from ^{15}N-Stable Isotopes. Environ. Sci. Technol. Lett., 9, 127–133, https://doi.org/10.1021/acs.estlett.1c00935, 2022.

Fuchs, H., Tan, Z., Lu, K., Bohn, B., Broch, S., Brown, S. S., Dong, H., Gomm, S., Häseler, R., He, L., Hofzumahaus, A., Holland, F., Li, X., Liu, Y., Lu, S., Min, K.-E., Rohrer, F., Shao, M., Wang, B., Wang, M., Wu, Y., Zeng, L., Zhang, Y., Wahner, A., and Zhang, Y.: OH reactivity at a rural site (Wangdu) in the North China Plain: contributions from OH reactants and experimental OH budget, Atmos. Chem. Phys., 17, 645–661, https://doi.org/10.5194/acp-17-645-2017, 2017.

Guo, H., Xu, L., Bougiatioti, A., Cerully, K. M., Capps, S. L., Hite, J. R., Carlton, A. G., Lee, S. H., Bergin, M. H., Ng, N. L., Nenes, A., and Weber, R. J.: Fine-particle water and pH in the southeastern United States, Atmos. Chem. Phys., 15, 5211–5228, https://doi.org/10.5194/acp-15-5211-2015, 2015.

Guo, H., Sullivan, A. P., Campuzano-Jost, P., Schroder, J. C., Lopez-Hilfiker, F. D., Dibb, J. E., Jimenez, J. L., Thornton, J. A., Brown, S. S., Nenes, A., and Weber, R. J.: Fine particle pH and the partitioning of nitric acid during winter in the northeastern United States, J. Geophys. Res.: Atmos., 121, https://doi.org/10.1002/2016jd025311, 2016.

Guo, H., Weber, R. J., and Nenes, A.: High levels of ammonia do not raise fine particle pH sufficiently to yield nitrogen oxide-dominated sulfate production, Sci. Rep., 7, 12109, https://doi.org/10.1038/s41598-017-11704-0, 2017.

Hao, Q., Jiang, N., Zhang, R., Yang, L., and Li, S.: Characteristics, sources, and reactions of nitrous acid during winter at an urban site in the Central Plains Economic Region in China, Atmos. Chem. Phys. 20, 7087–7102, https://doi.org/10.5194/acp-20-7087-2020, 2020.

Hu, B., Duan, J., Hong, Y., Xu, L., Li, M., Bian, Y., Qin, M., Fang, W., Xie, P., and Chen, J.: Exploration of the atmospheric chemistry of nitrous acid in a coastal city of southeastern China: results from measurements across four seasons, Atmos. Chem. Phys., 22, 371–393, https://doi.org/10.5194/acp-22-371-2022, 2022.

Hu, Q., Zhang, L., Evans, G. J., and Yao, X.: Variability of atmospheric ammonia related to potential emission sources in downtown Toronto, Canada, Atmos. Environ., 99, 365–373, https://doi.org/10.1016/j.atmosenv.2014.10.006, 2014.

Huang, R., Yang, L., Cao, J., Wang, Q., Tie, X., Ho, K., Shen, Z., Zhang, R., Li, G., Zhu, C., Zhang, N., Dai, W., Zhou, J., Liu, S., Chen, Y., Chen, J., and O'Dowd, C. D.: Concentration and sources of atmospheric nitrous acid (HONO) at an urban site in Western China, Sci. Total. Environ., 02, 165–172. https://doi.org/10.1016/j.scitotenv.2017.02.166, 2017.

Huy, D. H., Thanh, L. T., Hien, T. T., Noro, K., and Takenaka, N.: Characteristics of ammonia gas and fine particulate ammonium from two distinct urban areas: Osaka, Japan, and Ho Chi Minh City, Vietnam, Environ Environ. Sci. Pollut. Res. Int., 24, 8147–8163, https://doi.org/10.1007/s11356-017-8496-5, 2017.

Kleffmann, J., Kurtenbach, R., Lörzer, J., Wiesen, P., Kalthoff, N., Vogel, B., and Vogel, H.: Measured and simulated vertical profiles of nitrous acid—Part I: Field measurements, Atmos. Environ., 37, 2949–2955, https://doi.org/10.1016/s1352-2310(03)00242-5, 2003.

Kramer, L. J., Crilley, L. R., Adams, T. J., Ball, S. M., Pope, F. D., and Bloss, W. J.: Nitrous acid (HONO) emissions under real-world driving conditions from vehicles in a UK road tunnel, Atmos. Chem. Phys., 20, 5231–5248, https://doi.org/10.5194/acp-20-5231-2020, 2020.

Kurtenbach, R., Becker, K.H., Gomes, J.A.G., Kleffmann, J., Lorzer, J.C., Spittler, M., 510, and Wiesen, P., Ackermann, R., Geyer, A., Platt, U.: Investigations of emissions and heterogeneous formation of HONO in a road traffic tunnel, Atmos. Environ., 35, 3385-3394, https://doi.org/10.1016/S1352-2310(01)00138-8, 2001.

Li, D., Xue, L., Wen, L., Wang, X., Chen, T., Mellouki, A., Chen, J., and Wang, W.:

Characteristics and sources of nitrous acid in an urban atmosphere of northern China: Results from 1-yr continuous observations, Atmos. Environ., 182, 296–306, https://doi.org/10.1016/j.atmosenv.2018.03.033, 2018.

Li, S., Song, W., Zhan, H., Zhang, Y., Zhang, X., Li, W., Tong, S., Pei, C., Wang, Y., Chen, Y., Huang, Z., Zhang, R., Zhu, M., Fang, H., Wu, Z., Wang, J., Luo, S., Fu, X., Xiao, S., Huang, X., Zeng, J., Zhang, H., Chen, D., Gligorovski, S., Ge, M., George, C., and Wang, X.: Contribution of vehicle emission and NO_2 surface conversion to nitrous acid (HONO) in urban environments: Implications from tests in a tunnel, Environ. Sci. Technol., 55, 15616–15624, https://doi.org/10.1021/acs.est.1c00405, 2021.

Li, X., Brauers, T., Haseler, R., Bohn, B., Fuchs, H., Hofzumahaus, A., Holland, F., Lou, S., Lu, K.D., Rohrer, F., Hu, M., Zeng, L.M., Zhang, Y.H., Garland, R.M., Su, H., Nowak, A., Wiedensohler, A., Takegawa, N., Shao, M., and Wahner, A.: Exploring the atmospheric chemistry of nitrous acid (HONO) at a rural site in Southern China. Atmos. Chem. Phys., 12, 1497–1513, https://doi.org/10.5194/acp-12-1497-2012, 2012.

Liu, J., Liu, Z., Ma, Z., Yang, S., Yao, D., Zhao, S., Hu, B., Tang, G., Sun, J., Cheng, M., Xu, Z., and Wang, Y.: Detailed budget analysis of HONO in Beijing, China: Implication on atmosphere oxidation capacity in polluted megacity, Atmos. Environ., 244, https://doi.org/10.1016/j.atmosenv.2020.117957, 2021a.

Liu, M., Song, Y., Zhou, T., Xu, Z., Yan, C., Zheng, M., Wu, Z., Hu, M., Wu, Y., and Zhu, T.: Fine particle pH during severe haze episodes in northern China, Geophys. Res. Lett., 44, 5213–5221, https://doi.org/10.1002/2017gl073210, 2017.

Liu, P., Zhao, X., Zhang, C., Chen, H., Wang, J., Xue, L., Chen, J., and Mu, Y.: Fine particle pH and its influencing factors during summer at Mt. Tai: Comparison between mountain and urban sites, Atmos. Environ., 261, https://doi.org/10.1016/j.atmosenv.2021.118607, 2021.

Liu, Y., Ni, S., Jiang, T., Xing, S., Zhang, Y., Bao, X., Feng, Z., Fan, X., Zhang, L., and Feng, H.: Influence of Chinese New Year overlapping COVID-19 lockdown on HONO sources in Shijiazhuang, Sci. Total Environ., 745, 141025, http://10.1016/j.scitotenv.2020.141025,

2020a.

Liu, Y., Zhang, Y., Lian, C., Yan, C., Feng, Z., Zheng, F., Fan, X., Chen, Y., Wang, W., Chu, B., Wang, Y., Cai, J., Du, W., Daellenbach, K., Kangasluoma, J., Bianchi, F., Kujansuu, J., Petäjä, T., Wang, X., Hu, B., Wang, Y., Ge, M., He, H., and Kulmala, M.: The promotion effect of nitrous acid on aerosol formation in wintertime in Beijing: the possible contribution of traffic-related emissions, Atmos. Chem. Phys., 20, 13023–13040, https://10.5194/acp-20-13023-2020, 2020b.

Lv, S., Wang, F., Wu, C., Chen, Y., Liu, S., Zhang, S., Li, D., Du, W., Zhang, F., Wang, H., Huang, C., Fu, Q., Duan, Y., and Wang, G.: Gas-to-aerosol phase partitioning of atmospheric water-soluble organic compounds at a rural site in China: an enhancing effect of NH_3 on SOA formation. Environ. Sci. Technol., 56, 3915–3924, https://doi.org/10.1021/acs.est.1c06855, 2022.

Lyu, X., Wang, N., Guo, H., Xue, L., Jiang, F., Zeren, Y., Cheng, H., Cai, Z., Han, L., and Zhou, Y.: Causes of a continuous summertime O_3 pollution event in Jinan, a central city in the North China Plain, Atmos. Chem. Phys., 19, 3025–3042, https://doi.org/10.5194/acp-19-3025-2019, 2019.

Meng, F., Qin, M., Tang, K., Duan, J., Fang, W., Liang, S., Ye, K., Xie, P., Sun, Y., Xie, C., Ye, C., Fu, P., Liu, J., and Liu, W.: High-resolution vertical distribution and sources of HONO and NO_2 in the nocturnal boundary layer in urban Beijing, China, Atmos. Chem. Phys., 20, 5071–5092, https://doi.org/10.5194/acp-20-5071-2020, 2020.

Mikuska, P., Motyka, K., and Vecera, Z.: Determination of nitrous acid in air using wet effluent diffusion denuder–FIA technique, Talanta, 77, 635–641, https://doi.org/10.1016/j.talanta.2008.07.008, 2008.

Nah, T., Guo, H., Sullivan, A. P., Chen, Y., Tanner, D. J., Nenes, A., Russell, A., Ng, N. L., Huey, L. G., and Weber, R. J.: Characterization of aerosol composition, aerosol acidity, and organic acid partitioning at an agriculturally intensive rural southeastern US site, Atmos. Chem. Phys., 18, 11471–11491, https://doi.org/10.5194/acp-18-11471-2018, 2018.

Rumsey, I. C., Cowen, K. A., Walker, J. T., Kelly, T. J., Hanft, E. A., Mishoe, K., Rogers, C., Proost, R., Beachley, G. M., Lear, G., Frelink, T., and Otjes, R. P.: An assessment of the performance of the Monitor for aerosols and gases in ambient air (MARGA): a semi-continuous method for soluble compounds. Atmos. Chem. and Phys., 14, 5639–5658, https://doi.org/10.5194/acp-14-5639-2014, 2014.

Saraswati, Sharma, S. K., Saxena, M., and Mandal, T. K.: Characteristics of gaseous and particulate ammonia and their role in the formation of secondary inorganic particulate matter at Delhi, India, Atmos. Res., 218, 34–49, https://doi.org/10.1016/j.atmosres.2018.11.010, 2019.

Seinfeld, J. H., Pandis, S. N., and Noone, K. J.: Atmospheric chemistry and physics: from air pollution to climate change. Phys. Today, 51, 88–90, https://doi.org/10.1063/1.882420, 1998.

Shi, G., Xu, J., Peng, X., Xiao, Z., Chen, K., Tian, Y., Guan, X., Feng, Y., Yu, H., Nenes, A., and Russell, A. G.: pH of pH of aerosols in a polluted atmosphere: source contributions to highly acidic aerosol. Environ. Sci. Technol., 51, 4289–4296, https://doi.org/10.1021/acs.est.6b05736, 2017.

Shi, G., Xu, J., Shi, X., Liu, B., Bi, X., Xiao, Z., Chen, K., Wen, J., Dong, S., Tian, Y., Feng, Y., Yu, H., Song, S., Zhao, Q., Gao, J., and Russell, A. G.: Aerosol pH dynamics during haze periods in an urban environment in China: use of detailed, hourly, speciated observations to study the role of ammonia availability and secondary aerosol formation and urban environment. J. Geophys. Res. Atmos., 124, 9730–9742, https://doi.org/10.1029/2018jd029976, 2019.

Song, S., Gao, M., Xu, W., Shao, J., Shi, G., Wang, S., Wang, Y., Sun, Y., and McElroy, M. B.: Fine-particle pH for Beijing winter haze as inferred from different thermodynamic equilibrium models, Atmos. Chem. Phys., 18, 7423–7438, https://doi.org/10.5194/acp-18-7423-2018, 2018.

Su, H., Cheng, Y. F., Cheng, P., Zhang, Y. H., Dong, S., Zeng, L. M., Wang, X., Slanina, J.,

Shao, M., and Wiedensohler, A.: Observation of nighttime nitrous acid (HONO) formation at a non-urban site during PRIDE-PRD2004 in China, Atmos. Environ., 42, 6219–6232, https://doi.org/10.1016/j.atmosenv.2008.04.006, 2008.

Su, H., Cheng, Y., Oswald, R., Behrendt, T., Trebs, I., Meixner, F. X., Andreae, M. O., Cheng, P., Zhang, Y. H., and Poschl, U.: Soil nitrite as a source of atmospheric HONO and OH radicals, Science, 333, 1616–1618, https://10.1126/science.1208839, 2011.

Takeuchi M, M. Y., Tsunoda H, Tanaka H.: Atmospheric acid gases in tokushima, Japan, monitored with parallel plate wet denuder coupled ion chromatograph. Anal. Sci. 29, 165–168, https://doi.org/10.2116/analsci.29.165, 2013.

VandenBoer, T. C., Brown, S. S., Murphy, J. G., Keene, W. C., Young, C. J., Pszenny, A. A. P., Kim, S., Warneke, C., de Gouw, J. A., Maben, J. R., Wagner, N. L., Riedel, T. P., Thornton, J. A., Wolfe, D. E., Dubé, W. P., Öztürk, F., Brock, C. A., Grossberg, N., Lefer, B., Lerner, B., Middlebrook, A. M., and Roberts, J. M.: Understanding the role of the ground surface in HONO vertical structure: High resolution vertical profiles during NACHTT-11, J. Geophys. Res.: Atmos., https://doi.org/ 10.1002/jgrd.50721, 2013.

VandenBoer, T. C., Markovic, M. Z., Sanders, J. E., Ren, X., Pusede, S. E., Browne, E. C., Cohen, R. C., Zhang, L., Thomas, J., Brune, W. H., and Murphy, J. G.: Evidence for a nitrous acid (HONO) reservoir at the ground surface in Bakersfield, CA, during CalNex 2010. J. Geophys. Res.: Atmos., 119, 9093–9106, https://doi.org/10.1002/2013jd020971, 2014.

Veres, P., Roberts, J. M., Burling, I. R., Warneke, C., de Gouw, J., and Yokelson, R. J.: Measurements of gas-phase inorganic and organic acids from biomass fires by negative-ion proton-transfer chemical-ionization mass spectrometry., J. Geophys. Res.: Atmos., 115, D23302, https://doi.org/10.1029/2010jd014033, 2010.

Wang, G., Zhang, R., Gomez, M. E., Yang, L., Levy Zamora, M., Hu, M., Lin, Y., Peng, J., Guo, S., Meng, J., Li, J., Cheng, C., Hu, T., Ren, Y., Wang, Y., Gao, J., Cao, J., An, Z., Zhou, W., Li, G., Wang, J., Tian, P., Marrero-Ortiz, W., Secrest, J., Du, Z., Zheng, J., Shang, D., Zeng,

L., Shao, M., Wang, W., Huang, Y., Wang, Y., Zhu, Y., Li, Y., Hu, J., Pan, B., Cai, L., Cheng, Y., Ji, Y., Zhang, F., Rosenfeld, D., Liss, P. S., Duce, R. A., Kolb, C. E., and Molina, M. J.: Persistent sulfate formation from London Fog to Chinese haze. Proc. Natl. Acad. of Sci. U. S. A., 113, 13630–13635, https://doi.org/10.1073/pnas.1616540113, 2016a.

Wang, H., Ding, J., Xu, J., Wen, J., Han, J., Wang, K., Shi, G., Feng, Y., Ivey, C. E., Wang, Y., Nenes, A., Zhao, Q., and Russell, A. G.: Aerosols in an arid environment: the role of aerosol water content, particulate acidity, precursors, and relative humidity on secondary inorganic aerosols. Sci. Total Environ., 646, 564–572, https://doi.org/10.1016/j.scitotenv.2018.07.321, 2019.

Wang, M., Wang, S., Zhang, R., Yuan, M., Xu, Y., Shang, L., Song, X., Zhang, X., and Zhang, Y.: Exploring the HONO source during the COVID-19 pandemic in a megacity in China, J. Environ. Sci., 149, 616–627, https://doi.org/10.1016/j.jes.2023.12.021, 2025.

Wang, R., Ye, X., Liu, Y., Li, H., Yang, X., Chen, J., Gao, W., and Yin, Z.: Characteristics of atmospheric ammonia and its relationship with vehicle emissions in a megacity in China, Atmos. Environ. 182, 97–104, https://doi.org/10.1016/j.atmosenv.2018.03.047, 2018.

Wang, S., Wang, L., Li, Y., Wang, C., Wang, W., Yin, S., and Zhang, R.: Effect of ammonia on fine-particle pH in agricultural regions of China: comparison between urban and rural sites, Atmos. Chem. Phys. 20, 2719–2734, https://doi.org/10.5194/acp-20-2719-2020, 2020.

Wang, W., Wang, S., Xu, J., Zhou, R., Shi, C., and Zhou, B.: Gas-phase ammonia and $PM_{2.5}$ ammonium in a busy traffic area of Nanjing, China, Environ. Sci. Pollut. Res. Int., 23, 1691–1702, https://doi.org/10.1007/s11356-015-5397-3, 2016b.

Wang, X., Yin, S., Zhang, R., Yuan, M., and Ying, Q.: Assessment of summertime O_3 formation and the O_3-NO_X-VOC sensitivity in Zhengzhou, China using an observation-based model. Sci. Total Environ., 813, 152449, https://doi.org/10.1016/j.scitotenv.2021.152449, 2022.

Wang, Y., Zhu, S., Ma, J., Shen, J., Wang, P., Wang, P., and Zhang, H.: Enhanced atmospheric oxidation capacity and associated ozone increases during COVID-19 lockdown in the Yangtze River Delta, Sci. Total Environ., 768, 144796,

https://doi.org/10.1016/j.scitotenv.2020.144796, 2021.

Wong, K. W., Oh, H. J., Lefer, B. L., Rappenglück, B., and Stutz, J.: Vertical profiles of nitrous acid in the nocturnal urban atmosphere of Houston, TX, Atmos. Chem. Phys., 11, 3595–3609, https://doi.org/10.5194/acp-11-3595-2011, 2011.

Wu, S., Zhang, Y., Schwab, J., Li, Y., Liu, Y., and Yuan, C.: High-resolution ammonia emissions inventories in Fujian, China, 2009–2015, Atmos. Environ., 162, 100–114, https://doi.org/10.1016/j.atmosenv.2017.04.027, 2017.

Xu, W., Kuang, Y., Zhao, C., Tao, J., Zhao, G., Bian, Y., Yang, W., Yu, Y., Shen, C., Liang, L., Zhang, G., Lin, W., and Xu, X.: NH_3-promoted hydrolysis of NO_2 induces explosive growth in HONO, Atmos. Chem. Phys., 19, 10557–10570, https://doi.org/10.5194/acp-19-10557-2019, 2019.

Xu, Z., Wang, T., Wu, J., Xue, L., Chan, J., Zha, Q., Zhou, S., Louie, P. K. K., and Luk, C. W. Y.: Nitrous acid (HONO) in a polluted subtropical atmosphere: Seasonal variability, direct vehicle emissions and heterogeneous production at ground surface, Atmos. Environ., 106, 100–109, https://doi.org/10.1016/j.atmosenv.2015.01.061, 2015.

Yang, Y., Shao, M., Keßel, S., Li, Y., Lu, K., Lu, S., Williams, J., Zhang, Y., Zeng, L., Nölscher, A. C., Wu, Y., Wang, X., and Zheng, J.: How the OH reactivity affects the ozone production efficiency: case studies in Beijing and Heshan, China, Atmos. Chem. Phys., 17, 7127–7142, https://doi.org/10.5194/acp-17-7127-2017, 2017.

Yu, Y., Cheng, P., Li, H., Yang, W., Han, B., Song, W., Hu, W., Wang, X., Yuan, B., Shao, M., Huang, Z., Li, Z., Zheng, J., Wang, H., and Yu, X.: Budget of nitrous acid (HONO) at an urban site in the fall season of Guangzhou, China, Atmos. Chem. Phys., 22, 8951–8971, https://doi.org/10.5194/acp-22-8951-2022, 2022.

Yun, H., Wang, Z., Zha, Q., Wang, W., Xue, L., Zhang, L., Li, Q., Cui, L., Lee, S., Poon, S. C. N., and Wang, T.: Nitrous acid in a street canyon environment: Sources and contributions to local oxidation capacity, Atmos. Environ., 167, 223–234, https://doi.org/10.1016/j.atmosenv.2017.08.018, 2017.

Zellweger, M. A., P.Hofer,U.Baltensperger.: NOy speciation with a combined wet effluent diffusion denuder–aerosol collector coupled to ion chromatography, Atmos. Environ., 33, 1131–1140, https://doi.org/10.1016/s1352-2310(98)00295-7, 1999.

Zhang, Q., Liu, P., Wang, Y., Gerorge, C., Chen, T., Ma, S. L., Ren, Y., Mu, Y., Song, M., Herrmann, H., Mellouki, A., Chen, J., Zhao, X., Wang, S., and Y., Z.: Unveiling the underestimated direct emissions of nitrous acid (HONO), Proc. Natl. Acad. Sci. U.S.A., 120, https://doi.org/10.1073/pnas.2302048120, 2023

Zhang, S., Sarwar, G., Xing, J., Chu, B., Xue, C., Sarav, A., Ding, D., Zheng, H., Mu, Y., Duan, F., Ma, T., and He, H.: Improving the representation of HONO chemistry in CMAQ and examining its impact on haze over China, Atmos. Chem. Phys., 21, 15809–15826, https://doi.org/10.5194/acp-21-15809-2021, 2021.

Zhang, W., Tong, S., Jia, C., Wang, L., Liu, B., Tang, G., Ji, D., Hu, B., Liu, Z., Li, W., Wang, Z., Liu, Y., Wang, Y., and Ge, M.: Different HONO sources for three layers at the urban area of Beijing. Environ. Sci. Technol., 54, 12870–12880, https://doi.org/10.1021/acs.est.0c02146, 2020a.

Zhang, Y., Liu, X., Fang, Y., Liu, D., Tang, A., and Collett, J. L.: Atmospheric ammonia in Beijing during the COVID-19 outbreak: concentrations, sources, and implications. Environ. Sci. Technol. Lett. 8, 32–38, https://doi.org/10.1021/acs.estlett.0c00756, 2020b.

Zhao, Y., Zhang, N., Wei, Q., Han, Y., Mao, K., Cai, Y., and Li, R.: Flow injection chemiluminescence method in analytical chemistry., Spectrosc. Spectra. Anal., 30, 2512–2517., https://doi.org/11-2200/O4WCNKI, 2010.